

**U.S. DEPARTMENT OF COMMERCE  
National Technical Information Service**

**AD-A030 883**

**Analytical and Experimental  
Investigations of Delta Wings in  
Incompressible Flow**

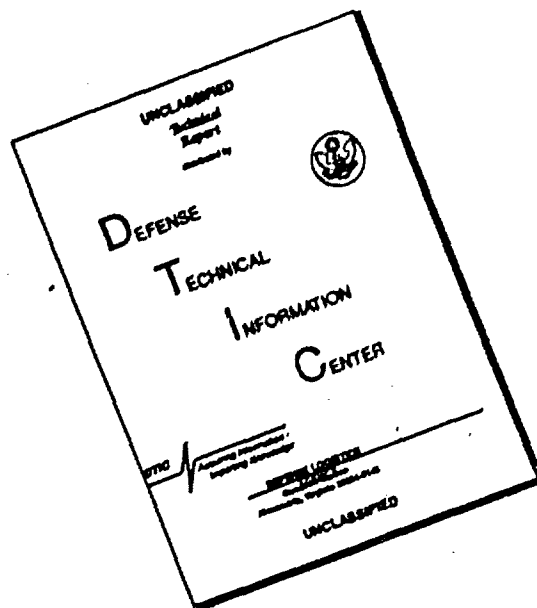
**Texas A and M Research Foundation College Station**

**Prepared for**

**Office of Naval Research, Arlington, Va**

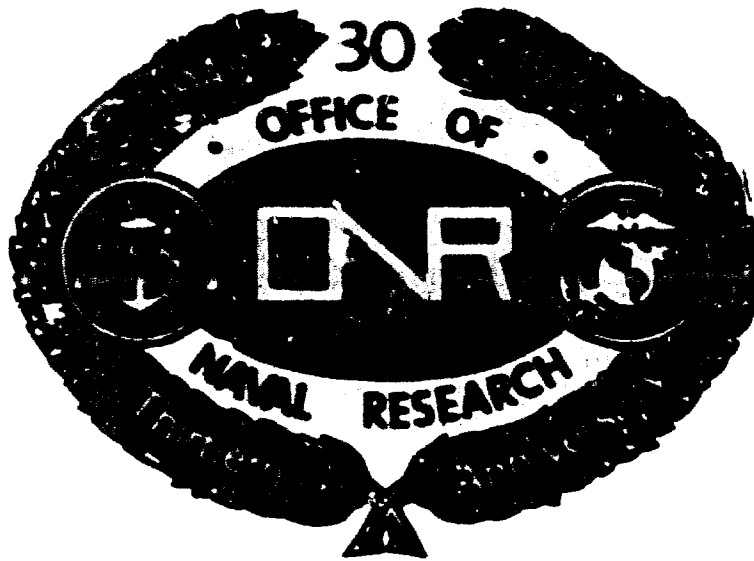
**Aug 76**

# DISCLAIMER NOTICE



THIS DOCUMENT IS BEST QUALITY AVAILABLE. THE COPY FURNISHED TO DTIC CONTAINED A SIGNIFICANT NUMBER OF PAGES WHICH DO NOT REPRODUCE LEGIBLY.

AD A 030883



**ANALYTICAL AND EXPERIMENTAL INVESTIGATIONS OF  
DELTA WINGS IN INCOMPRESSIBLE FLOW**

Balusu M. Rao  
James K. Nathman

Texas A&M Research Foundation  
F. E. Box H  
College Station, TX 77843

Contract N00014-75-C-0255  
ONR Task 215-231

August 1976

Interim Report for the Period 1 January - 31 December 1976

Approved for public release; distribution unlimited.

PREPARED FOR THE



DEPARTMENT OF THE NAVY  
OFFICE OF NAVAL RESEARCH  
TECHNOLOGY PROJECTS DIVISION  
Vehicle Technology, Code 211  
Arlington, Virginia 22217

REPRODUCED BY  
NATIONAL TECHNICAL  
INFORMATION SERVICE  
U. S. DEPARTMENT OF COMMERCE  
SPRINGFIELD, VA. 22161

DDC  
RECEIVED  
OCT 19 1976  
REGISTRY  
D

REPORT DOCUMENTATION PAGE		READ INSTRUCTIONS BEFORE COMPLETING FORM	
1. REPORT NUMBER	2. GOVT ACCESSION NO.	3. RECIPIENT'S CATALOG NUMBER	
4. TITLE (and Subtitle)		5. TYPE OF REPORT & PERIOD COVERED	
Analytical and Experimental Investigations of Delta Wings in Incompressible Flow		Jan 1975 - Dec 1975 Final Technical Report	
6. AUTHOR		6. PERFORMING ORG. REPORT NUMBER	
W. M. Rao and S. Nathman		8. CONTRACT OR GRANT NUMBER(s)	
		NR0014-75-C-0255	
9. PERFORMING ORGANIZATION NAME AND ADDRESS		10. PROGRAM ELEMENT, PROJECT, TASK AREA & WORK UNIT NUMBERS	
Texas A&M Research Foundation P. O. Box H College Station, TX 77843		NR 215-231	
11. CONTROLLING OFFICE NAME AND ADDRESS		12. REPORT DATE	
Office of Naval Research Vehicle Technology Programs, Code 211 Arlington, VA 22217		August 1976	
		13. NUMBER OF PAGES	
		91	
14. DISTRIBUTING AGENCY NAME & ADDRESS (if different from Controlling Office)		15. SECURITY CLASS. (of this report)	
		Unclassified	
		15a. DECLASSIFICATION/DOWNGRADING SCHEDULE	
16. DISTRIBUTION STATEMENT (of this Report)			
Approved for public release; distribution unlimited. Reproduction in whole or in part is permitted for any purpose of the United States Government.			
17. DISTRIBUTION STATEMENT (of the abstract entered in Block 20, if different from Report)			
18. SUPPLEMENTARY NOTES			
<b>BEST AVAILABLE COPY</b>			
19. KEY WORDS (Continue on reverse side if necessary and identify by block number)			
Vortex Flows; Leading Edge Separation; Delta Wings; Subsonic Flows; Numerical Lifting Surface Theory; Wing Vortex Interaction			
20. ABSTRACT (Continue on reverse side if necessary and identify by block number)			
The theoretical analysis of delta wings in incompressible flow is created by a numerical lifting-surface theory based upon a velocity potential formula- tion. This theory has been expanded to include spanwise velocity effects and the leading-edge separation associated with delta wings. The numerical technique has made use of both fixed and free wakes. In the fixed-wake model, the ana- lytical results of Brown and Michael have been used to position the leading edge vortex. In the more refined free-wake model, the leading edge separation was modeled as a discrete number of vortices attached to the leading-edge, which are			

allowed to align themselves with streamlines. The iteratively determined position of these vortices resembles the experimentally-observed spiral form, while computed lift coefficients reflect the added vortex lift.

Experimental research included wind tunnel tests to determine the vortex location, vortex burst location, and upper surface pressure distribution on a delta wing,  $M = 2$ , in an oscillatory airstream. In steady flow, an axisymmetric "tulip" type burst was observed at all angles of attack; while in unsteady flow, the vortex core gradually dissipated into turbulence for increasing angles of attack but formed a "helical" type of burst for decreasing angles. The pressure distributions showed that in unsteady flow, there were considerable phase lags in the suction peaks associated with the vortices but virtually no lags elsewhere on the wing.



ANALYTICAL AND EXPERIMENTAL INVESTIGATIONS OF  
DELTA WINGS IN INCOMPRESSIBLE FLOW

Balusu M. Rao  
James K. Nathman

Texas A&M Research Foundation  
F. E. Box H  
College Station, TX 77843

Contract N00014-75-C-0255  
ONR Task 215-231

August 1976

Interim Report for the Period 1 January - 31 December 1976

Approved for public release; distribution unlimited.

PREPARED FOR THE

DEPARTMENT OF THE NAVY  
OFFICE OF NAVAL RESEARCH  
TECHNOLOGY PROJECTS DIVISION  
Vehicle Technology, Code 211  
Arlington, Virginia 22217



ACC 00 24 ✓

A

11

### Change of Address

Organizations receiving reports on the initial distribution list should confirm correct address. This list is located at the end of the report. Any change of address or distribution should be conveyed to the Office of Naval Research, Code 211, Arlington, VA 22217.

### Disposition

When this report is no longer needed, it may be transmitted to other organizations. Do not return it to the originator or the monitoring office.

### Disclaimer

The findings and conclusions contained in this report are not to be construed as an official Department of Defense or Military Department position unless so designated by other official documents.

### Reproduction

Reproduction in whole or in part is permitted for any purpose of the United States Government.

## ABSTRACT

The theoretical analysis of delta wings in incompressible flow is treated by a numerical lifting-surface theory based upon a velocity potential formulation. This theory has been expanded to include spanwise velocity effects and the leading-edge separation associated with delta wings. The numerical technique has made use of both fixed and free wakes. In the fixed-wake model, the analytical results of Brown and Michael have been used to position the leading-edge vortex. In the more refined free-wake model the leading-edge separation was modeled as a discrete number of vortices attached to the leading-edge, which are allowed to align themselves with streamlines. The iteratively determined position of these vortices resembles the experimentally-observed spiral form, while computed lift coefficients reflect the added vortex lift.

Experimental research included wind tunnel tests to determine the vortex location, vortex burst location, and upper surface pressure distribution on a delta wing,  $AR = 2$ , in an oscillatory airstream. In steady flow, an axisymmetric 'tulip' type burst was observed at all angles of attack; while in unsteady flow, the vortex core gradually dissipated into turbulence for increasing angles of attack but formed a 'helical' type of burst for decreasing angles. The pressure distributions showed that in unsteady flow, there were considerable phase lags in the suction peaks associated with the vortices but virtually no lags elsewhere on the wing.

## FOREWARD

The work described in this technical report was performed by Texas A&M Research Foundation for the Department of the Navy, Office of Naval Research, Arlington, Virginia under contract number N00014-75-C-0255. The Scientific Officer who initiated this research program was Mr. Thomas L. Wilson and he was followed by CDR William Albers. The present Scientific Officer of the program is Dr. Robert Whitehead and the Director of the Vehicle Technology program is Mr. Dave S. Siegel. The investigators responsible for the theoretical and experimental research were Mr. James K. Nathman and Dr. A. G. Parker, respectively.

TABLE OF CONTENTS

REPORT DOCUMENTATION PAGE	i
ABSTRACT	iii
FORWARD	v
TABLE OF CONTENTS	vii
LIST OF ILLUSTRATIONS	viii
NOMENCLATURE	viii
INTRODUCTION	x
I. THEORETICAL INVESTIGATION	6
Aerodynamic Theory	6
Numerical Applications and Results	11
Attached Flow Model	11
Calculation of Pressure Distribution	13
Fixed-wake Model	14
Free-wake Model	16
Convergence	17
Results	20
Future Improvements	24
Conclusions	25
II. EXPERIMENTAL INVESTIGATION	27
Equipment and Tests	27
Discussion	28
1) Flow Visualization	28
a) Steady Flow	28
b) Oscillatory Flow	29
2) Pressure Measurements	30
Conclusions	31
REFERENCES	32

## LIST OF ILLUSTRATIONS

<u>Figure</u>		<u>Page</u>
1	Flow over Delta wing	40
2	Model of Brown and Michael	41
3	Model of Mangler and Smith	42
4	Vortex Lattice of Kandil, Mook, and Nayfeh	43
5	Panel Model of Weber	44
6	Polhamus' Lift Constants	45
7	Equivalent of Doublet Panel and Vortex Box	46
8	Velocity Oriented Coordinate Axes	47
9	Generation of Wake Strips	47
10	Addition of Wake Influence to Edge Box	48
11	Sign Convention	49
12	Attached Flow Model	50
13	Duplication of Brown and Michael	51
14	$C_L$ vs. $\alpha$ predicted by the Fixed-Wake Model	52
15	Center of Pressure Predicted by the Fixed-Wake Model	53
16	Comparison of Pressure Distribution Predicted for the Fixed-Wake Model and Experimental Results	54
17	Free-Wake Model of Leading Edge Sheet	55
18	Trailing Edge of Free-Wake Model	56
19	Polar Coordinate System	57
20	Free-Wake Geometry Prediction	58
21	Finite-Size Core	58
22	Vortex Core Position of Smith	59
23	Auxiliary Point Placement	60
24	Lift Curve of Free-Wake Model	61
25	Lift Curve of Free-Wake Model	62

## LIST OF ILLUSTRATIONS

<u>Figure</u>		<u>Page</u>
26	Center of Pressure Predicted by Free-Wake Model	63
27	Free-Wake Model Loading Distribution	64
28	Converged Leading-Edge Sheet Geometry	65
29	Details of Test Equipment	66
30	Gust Generator and Airfoil	67
31	Vortex Flow Visualization-Steady Flow	68
32	Vortex Flow Visualization - $k=0.2$	69
33	Vortex Flow Visualization - $k=0.4$	70
34	Details of a Helical Type Burst	71
35	Vortex Burst-Steady Flow	72
36	Location of Pressure Ports	73
37	Pressure Distribution on a Delta Wing	74
38	Vortex Burst - $k=0.2$	80
39	Vortex Burst - $k=0.4$	81

## NOMENCLATURE

- $\alpha$  - attack angle  
 $A$  - area of vortex box  
 $AR$  - aspect ratio  
 $b$  - wing span  
 $c$  - contour variable  
 $\bar{c}$  - mean aerodynamic chord ( $=2/3 c_R$ )  
 $c_R$  - root chord  
 $C$  - aerodynamic influence coefficient  
 $C_L$  - lift coefficient  
 $C_N$  - normal force coefficient  
 $D$  - flow field domain  
 $k$  - reduced frequency ( $=\frac{\omega \bar{c}}{V}$ )  
 $\kappa$  - doublet strength  
 $K_p$  - potential lift constant  
 $K_v$  - vortex lift constant  
 $n$  - surface normal  
 $P$  - field point  
 $Q$  - boundary surface point  
 $r$  - distance between  $P$  and  $Q$   
 $s$  - local wing semi-span  
 $S$  - boundary surface variable  
 $t$  - time  
 $V$  - velocity  
 $WRALPH$  - ratio of wake inclination angle to angle of attack  
 $(S_1, S_2, S_3)$  - velocity oriented, normal surface axes

$(u, v, w)$  - Cartesian velocities

$(u, u_\theta, u_R)$  - polar velocities

$(x, y, z)$  - Cartesian coordinates

$(x, \theta, R)$  - polar coordinates

$(X_V, Y_V, Z_V)$  - coordinates of vortex core endpoint

$\Delta C_p$  - loading coefficient

$\Delta P$  - pressure differential across surface

$\alpha$  - angle of attack

$\epsilon$  - wing semi-apex angle

$\gamma$  - vorticity

$\phi$  - perturbation velocity potential

$\omega$  - angular velocity

Subscripts:

$l$  - lower surface

$n$  - normal

$u$  - upper surface

$s$  - surface

$(U, V, W)$  influence coefficient subscripts - influence coefficients of

$(u, v, w)$  velocities

$W$  - wing

$V$  (matrix subscripts) - LE vortex sheet

TE - TE vortex sheet

## INTRODUCTION

Since 1974 the Office of Naval Research (ONR) has been conducting an in-depth study of vortex flows. The aim of this study is the understanding of the interaction between wings and vortex flow systems. From the understanding will come advances in stall and buffet boundaries, and increased performance for VTOL and STOL craft. Texas A&M University is under contract to ONR to investigate theoretically and experimentally the flow over delta wings. This report includes a complete account of the research findings.

A delta wing is considered the starting point in investigating the potential benefits of leading-edge separation because of its simple planform and because the vortex flow over the wing is created by self-induced separation. In addition, abundant experimental evidence is available to evaluate theoretical predictions and to indicate aspects requiring special attention, theoretically or experimentally.

The available experimental evidence leads one to believe the flow over a delta wing is as shown in Figure 1. The upper and lower surface boundary layers separate from the wing along each leading edge to form free shear layers. These shear layers then roll up into spiral vortices lying above and inboard of the leading edges. The suction peak on the wing below the primary vortex leads to secondary and perhaps tertiary separations. The vortex-induced suction results in increased lift. The vortex-induced lift is nonlinear with respect to angle of attack and is not readily predicted by linear potential flow theories.

A complete summary of the theoretical and experimental investigations into the flow about delta wings has been compiled by Matoi.<sup>14</sup>

Correct modelling of the flow should include the effects of the primary vortex, secondary vortex, and viscous effects. However, experimental evidence (some of which has been collected at Texas A&M University) and the success of theories which neglect all but the effect of the primary vortex suggest only the first phenomenon need be included in the theoretical model.

The theoretical investigation into the effect of leading-edge separation on delta wings spans over a quarter century. In 1946, P. T. Jones<sup>2</sup>, using slender wing theory, postulated that low aspect ratio wings would have a lift slope of  $-AR/2$ . This value is only slightly conservative at low angles of attack but since the theory neglects vortex lift, predicted lift falls increasingly below experimental lift as the angle of attack increases.

Legendre<sup>3</sup> in 1952 was the first to include the effect of leading-edge flow separation on delta wings and ascribe the significant increase in lift-slope to this phenomenon. Using conical flow theory (as do most analytic theories developed for delta wings) Legendre reduced the region under consideration to the cross-flow plane and modeled the primary vortex sheets as two point vortices lying above the wing. The position and strength of these vortices were determined by requiring no force on each vortex and a smooth flow off the leading edge.

Brown and Michael<sup>4</sup> expanded Legendre's concept by adding straight vortex feeder sheets extending from the leading edge to the isolated vortices, as seen in Figure 2. These sheets accounted for the increasing strength of the primary vortices. Brown and Michael positioned the primary vortices such that the isolated vortex and feeder sheet combined were under no net force.

Mangler and Smith<sup>5</sup> and later Smith<sup>6</sup> and Pullin<sup>7</sup> allowed each feeder sheet to deform into a spiral which asymptotically approaches the vortex core (Figure 3). The free-surface condition on the leading-edge vortex sheets was more rigorously applied by separately requiring no force to be sustained by the core and no pressure discontinuity at a finite number of points on the sheet. Smith's work is especially note-worthy since he could easily vary the extent of the leading-edge sheet outside the vortex core.

Nangia and Hancock<sup>8</sup> in 1968 were the first to apply three-dimensional numerical lifting-surface theory to delta wings using the model of Brown and Michael for the leading-edge separation. Their procedure involved a collocation method for determining the Fourier coefficients for the assumed series distribution of vorticity over the wing. Their theory did include the Kutta condition at the trailing edge and, hence, is a departure from the conical flow assumption of analytic theories.

Mook and Maddox<sup>9</sup>, Kandil, Mook and Nayfeh<sup>10</sup> and Rehbach<sup>11</sup> represented the leading-edge separation as a system of discrete vortices which are aligned with streamlines (Figure 4). Although accurate in their prediction of lift coefficients, the success of Kandil et. al. at reproducing the experimentally observed vortex shape does not lend confidence to their empirical procedure.

Most recently, Weber, et. al.<sup>12</sup> applied a potential flow computational technique to the problem, representing the wing, rolled-up vortex sheets and the wake by piecewise continuous, quadratically-varying strength doublet panels (Figure 5). Their technique allows the tangent flow and free-surface conditions to be applied independently to the appropriate panels, and hence,

satisfy the Kutta condition at the leading and trailing edges.

Finally, Polhamus'<sup>13</sup> concept should be mentioned, not for its rigorous mathematical justification, but because of the accuracy and simplicity of its prediction of the lift of delta wings. The concept is based on an analogy between the vortex lift and the leading-edge suction associated with the potential flow about the leading edge. Polhamus defines the lift of a wing with leading-edge separation as:

$$C_L = K_p \sin \alpha \cos^2 \alpha + K_v \sin^2 \alpha \cos \alpha$$

The values of  $K_p$  and  $K_v$  are only functions of aspect ratio and can be determined by linear potential flow theory. Graphs of them for delta wings are given in Figure 6.

Aerodynamic data on wings of low aspect ratio (of order 1) delta wings with sharp leading edges is well documented.<sup>(27-31)</sup> Data on wings of Aspect ratio 1.5 and above is considerably more scarce and data for unsteady flow past these wings virtually non existent.

The steady flow is characterized by two vortices, caused by leading edge separation, which lie above the wing close to the leading edges. With increasing angle of attack these vortices increase in strength and move inboard causing two large suction peaks in the spanwise loading. At some point along the length of the vortices the phenomena of vortex breakdown i.e. the bursting of the tightly rolled vortex core, occurs. At moderate angles of attack this is well downstream of the trailing edge of the wing but with increasing angle the burst point moves rapidly forward until it occurs above the wing producing unsteadiness in the loading.<sup>(32-37)</sup> Increasing the aspect ratio causes the burst to reach the trailing edge at lower angles of attack.

Two distinct types of breakdown have been observed<sup>(33,34)</sup>, one more common at high Reynolds numbers is an axisymmetric burst where the core suddenly expands to form a "tulip" shaped "bubble". In the other, more generally seen at low Reynolds numbers, the core has a sharp kink and starts swirling in a helical path about its axis before breaking down into turbulence.

In unsteady flow the vortex cores move both laterally and vertically and their loci have been measured during various motions for low aspect ratio wings<sup>(38-42)</sup>. However as yet no effort has been made to ascertain the effect of flow unsteadiness on vortex bursting or to determine the effect of the burst on the transient loading. The current tests were planned to investigate these areas.

## I. THEORETICAL INVESTIGATION

### Aerodynamic Theory

Steady, inviscid, irrotational, and incompressible fluid flow is characterized by a perturbation velocity potential  $\phi(P)$  satisfying Laplace's equation, i.e.:

$$\nabla^2 \phi = 0 \quad (1)$$

Green's theorem relates the value of  $\phi(P)$  inside a domain  $D$  (i.e.  $P \in D$ ) to the value of  $\phi$  and its normal derivative,  $\frac{\partial \phi}{\partial n}$ , on the fluid boundary  $S$ :

$$\phi(P) = \int_S \frac{\partial \phi(Q)}{\partial n_S} \left( -\frac{1}{4\pi r} \right) dS + \int_S \phi(Q) \frac{\partial}{\partial n_S} \left( \frac{1}{4\pi r} \right) dS \quad (2)$$

where  $r$  is the scalar distance between the surface point  $Q$  and  $P$ . If the boundary  $S$  is a two-dimensional surface, then we may combine the integration over the upper and lower surfaces as:

$$\begin{aligned} \phi(P) = & \int_{\bar{S}} \left( \frac{\partial \phi_U}{\partial n_U} + \frac{\partial \phi_L}{\partial n_L} \right) \left( -\frac{1}{4\pi r} \right) d\bar{S} \\ & + \int_{\bar{S}} \left( \phi_U \frac{\partial}{\partial n_U} \left( \frac{1}{4\pi r} \right) + \phi_L \frac{\partial}{\partial n_L} \left( \frac{1}{4\pi r} \right) \right) d\bar{S} \end{aligned} \quad (3)$$

where the bar over the surface variable indicates integration over one side of the boundary.

But  $n_U = -n_L$ , and for tangential flow to occur on the upper and lower surfaces:

$$\frac{\partial \phi_U}{\partial n_U} = - \frac{\partial \phi_L}{\partial n_L} \quad (4)$$

Then the velocity potential can be written in terms of its upward normal derivative as:

$$\phi(P) = \int_S (\phi_u - \phi_l) \frac{\partial}{\partial n_u} \left( \frac{1}{4\pi r} \right) dS \quad (5)$$

The velocity induced at a point is the gradient of the perturbation velocity potential,  $\nabla\phi(P)$ . Since this operation is performed in the domain  $D$ , the operator can be brought inside the boundary integration. Introducing  $K$  as the discontinuity in potential between the lower and upper surfaces,

$$K = \phi_l - \phi_u \quad (6)$$

then the induced velocity can be written:

$$V(P) = - \int_S \nabla \frac{K}{4\pi} \frac{\partial}{\partial n} \left( \frac{1}{r} \right) dS \quad (7)$$

If  $S$  is divided into a number of small subregions  $S_j$ , such that  $K$  can be considered constant within these subregions then:

$$V(P) = \sum_j \frac{K_j}{4\pi} \left( - \int_{S_j} \nabla \frac{\partial}{\partial n} \left( \frac{1}{r} \right) dS \right) \quad (8)$$

The surface integral over each subregion has been shown (Ref. 15) to be equivalent to a contour integration around the subregion. Further, this contour integration represents the influence of a vortex filament of unit strength on the contour of the subregion, as illustrated in Figure 7. The contour integral,

$$C_{ij} = - \int_{C_j} c \times \nabla \left( \frac{1}{r} \right) dc = - \int_{S_j} \nabla \frac{\partial}{\partial n} \left( \frac{1}{r} \right) dS \quad (9)$$

becomes the vector aerodynamic influence coefficient of subregion  $j$  on the point  $P_i$ . Using the subscript  $i$  of  $V$  to denote the velocity induced at the point  $P_i$ , the total induced velocity is written:

$$V_i = \frac{1}{4\pi} \sum_j K_j C_{ij} \quad (10)$$

In matrix notation, the velocities at several points are:

$$\{V\} = \frac{1}{4\pi} [C] \{K\} \quad (11)$$

For the induced velocity field given by (11) to be accurate, the aerodynamic influence matrix must adequately represent the lifting surface by including all of the surface over which a discontinuity in potential exists, sufficiently approximate the geometry of the surface, and be consistent with the assumption that  $K$  is constant within each subregion.

The distribution of  $K$  over the surface is determined by three conditions - undisturbed flow at infinity, tangent flow over the boundary, and no pressure discontinuity across a free surface. The condition of undisturbed flow at infinity is implicit in the Green's theorem derivation of the potential equation. It can also be interpreted as meaning  $K$  is zero upstream of the leading stagnation point. When  $K$  is so specified, the influence coefficients of the stream surface upstream of the leading stagnation point need not be calculated.

Over the wing and wake, the flow must be tangent to the lifting surface, i.e., the net velocity normal to the surface must be zero. The free-stream velocity component normal to the surface at point  $Q_i$  is:

$$(V_{n\infty})_i = n_i \cdot V_\infty \quad (12)$$

and the induced normal velocity at point  $Q_i$  is:

$$(V_n)_i = \frac{1}{4\pi} [n_i \cdot C_j] \{K\} = \frac{1}{4\pi} [C_n]_i \{K\} \quad (13)$$

For the net normal velocity to be zero, the induced velocity must be the negative of the freestream component, i.e.,

$$[C_n]_i \{K\} = -4\pi (n_i \cdot V_\infty) \quad (14)$$

For several collocation points at which the tangent flow condition is satisfied.

$$[C_n] \{K\} = -4\pi \{n \cdot V_\infty\} \quad (15a)$$

The aerodynamic influence matrix,  $[C_n]$ , can be calculated from the known geometry of the lifting surface, while the freestream velocity and surface normals are also specified. Thus, using as many collocation points as unknown  $K_i$ , the doublet distribution over the surface can be computed.

Usually, each subregion of the surface is provided with its own collocation point located near the centroid of the subregion. Empirical schemes,<sup>16,17</sup> with and without justification have been used to strategically place the control points at positions other than the centroid. These alternate positions can improve a program's results, since the location of the collocation point within the vortex box can effect the doublet strength of the box.

The third condition which the free portions of the lifting surface must meet is that of no pressure differential across the surface. The vorticity on the surface is given by the gradient of the discontinuity in potential:

$$\gamma = n \times (V_l - V_u) = n \times \nabla K \quad (16)$$

The loading on the surface is:

$$\Delta P = \rho V \times \gamma \quad (17)$$

from which the loading coefficient is

$$\Delta C_p = 2 \frac{V}{V_\infty} \times \frac{\gamma}{V_\infty} \quad (18a)$$

$$= 2 \frac{V}{V_\infty} \times (n \times \nabla) \frac{K}{V_\infty} \quad (18b)$$

$$\Delta C_p = \frac{2}{V_\infty^2} \left( u \frac{\partial K}{\partial x} + v \frac{\partial K}{\partial y} + w \frac{\partial K}{\partial z} \right) \quad (18c)$$

If a set of axes ( $S_1, S_2, S_3$ ) is placed on a free doublet surface and oriented with the velocity vector as shown in Figure 8. Then:

$$\begin{aligned} \mathbf{v} &= |V| \hat{S}_1 \\ \mathbf{n} &= S_3 \\ \mathbf{v} &= \frac{\partial}{\partial S_1} \hat{S}_1 + \frac{\partial}{\partial S_2} \hat{S}_2 + \frac{\partial}{\partial S_3} \hat{S}_3 \\ \mathbf{n} \times \mathbf{v} &= -\frac{\partial}{\partial S_2} \hat{S}_1 + \frac{\partial}{\partial S_1} \hat{S}_2 \\ \Delta C_p &= \frac{2}{V_\infty^2} |V| \frac{\partial K}{\partial S_1} \hat{S}_3 \end{aligned} \quad (18d)$$

For a free surface  $\Delta C_p = 0$ , therefore,

$$\frac{\partial K}{\partial S_1} = 0 \quad (19)$$

From (19), it is apparent that on a free surface,  $K$  is constant along a streamline. Thus, in steady flow, the doublet strength at a point  $Q$  in the wake equals the doublet strength at the trailing edge point upstream of  $Q$ . This is merely a restatement of the requirement that free vorticity be aligned along a streamline in steady flow. More importantly, it also implies that if two sides of the subregions on a free surface coincide with streamlines, the subregions degenerate into semi-infinite strips. This is illustrated in Figure 9.

Instead of providing collocation points in the wake and using the tangent flow condition to solve for the  $K$  distribution in the wake, the influence of the wake strips may be added to the appropriate edge subregions, boxes, (as seen in Figure 10) since their strengths are equal. This

is desirable numerically since it reduces the number of simultaneous equations to be solved.

Another numerical simplification results from symmetry conditions. Whenever one box (the image) is known to have the same strength as another (primary) box, the influence of the image box can be added to the influence of the primary box. This simplification can result from symmetry such as that occurring between right and left wings of an aircraft in straight, level flight. Such symmetry includes the tangent flow condition which need only be applied to the primary box.

For a high-aspect ratio, planar wing in rectilinear flight, it has been found necessary to rigidly enforce both the tangent-flow and free-surface conditions on the trailing wake.<sup>18</sup> In such cases, wake roll-up can be neglected and a planar wake consisting of semi-infinite strips trailing back in the x direction can be assumed.

### Numerical Applications and Results

#### Attached Flow Model

The lifting-surface theory is applied numerically to delta wings using the sign convention shown in Figure 11. The wing lies in the x-y plane with the x axis pointing aft along the line of symmetry. For a wing as described, the normal vector is  $\hat{k}$  which makes the particular equations for tangent flow and loading coefficient:

$$[C_w] : K = -4\pi (w_\infty) \quad (15b)$$

$$C_p = \frac{2}{V_\infty^2} \left( u \frac{\partial K}{\partial x} + v \frac{\partial K}{\partial y} \right) \quad (18e)$$

where the symbols (u,v,w) refer to the Cartesian velocity components.

The wing is divided into subregions (vortex boxes) by chordwise and spanwise lines which divide the interior of the wing into rectangles and form triangles at the leading edge, as shown in Figure 12. Collocation points lie along spanwise lines, halfway between the left and right sides of the boxes. These positions which are the centroids of the rectangles, but not of the triangles were employed to facilitate the calculation of the gradient of the doublet strength. Comparison of results using this scheme and one using the centroids of the leading-edge triangles as collocation points yielded negligible changes.

By adding a wake consisting of semi-infinite extensions of the chordwise lines, an attached flow (without leading-edge separation) model resulted. This model was made more realistic by allowing the planar trailing-edge wake to incline upwards at an angle described in terms of the ratio of wake inclination angle to angle attack ( $WKALPH$ ). For values of this ratio between zero and unity, negligible changes in lift resulted. For the results to be presented in this study, this ratio has been set at one-half following Gersten<sup>19</sup> and Bollay<sup>20</sup>.

The computed lift slope of this model was within 5% of that calculated for Polhamus' potential flow model when an 8 x 8 grid (36 boxes on each half-wing) was used, and within 1% when a 10 x 10 grid (55 boxes) was used. Thus, a model with a 10 x 10 grid has been used for the reported computations.

Two models of the leading-edge separation are presented here. One is a fixed-wake model, where a simplified form of the primary vortex is assumed and the pressure distribution is calculated without checking the correctness of the assumption. This model is designated the Brown and Michael model since it closely matches their assumed form and uses, indirectly,

their analytical calculations. The second model is, to a large extent, a free-wake model. That is, a guess is made of the shape and strength of the leading-edge vortex sheet; and this guess is iterated to improve the leading-edge sheet until it satisfies the tangent-flow and free-surface conditions. This model in some respects matches that of Mangler and Smith and also uses, indirectly, the analytic calculations of Smith.

#### Calculation of Pressure Distribution

For a planar lifting surface, such as the attached flow model, the loading at any point is dependent on  $\partial K/\partial x$  and the lift per unit span is proportional to the doublet strength at the trailing edge. This is true because the tangential velocity over the lifting surface is constant. The primary vortex sheets of a delta wing, though, induce significant velocities which vary over the wing. For each point at which the loading is to be computed, the two-dimensional gradient of the doublet strength and the tangential velocities must be found as suggested by Equation 18e.

At present the gradient is calculated using three-point finite differences. These differences use the position of the collocation points and their associated  $K$  values. For points near the edges of the wing, either forward or backward differences are used, and the symmetry condition  $\partial K/\partial y = 0$  is incorporated at points near the centerline.

The induced velocities are calculated using the influence of the leading-edge sheet only, since the planar wing cannot induce tangential velocities on itself and the influence of the trailing-edge wake is assumed to be small.

The normal force coefficient is the integrated loading distribution, which is approximated by:

$$C_N = \frac{\sum_i \Delta C_{p_i} A_i}{\sum_i A_i} \quad (20)$$

where  $A_i$  is the area of each box.

The lift is then:

$$C_L = C_N \cos \alpha \quad (21)$$

Similarly, the moment about the y axis is:

$$C_{MLE} = \frac{-\sum_i \Delta C_{p_i} A_i x_i}{\sum_i A_i \bar{c}} \quad (22)$$

where the location of the collocation point is used for the moment arm ( $x_i$ ) of each box.

#### Fixed-Wake Model

The model of Brown and Michael was duplicated by placing a series of planar boxes along the leading edge which extend to the position of the vortex core predicted analytically by Brown and Michael. (See Figure 13.) The box sides extending from the leading edge are perpendicular to it and represent the feeder vortices of Brown and Michael. The sides of the boxes opposite the leading edge form two concentrated vortices representing the primary vortex system. Experimental observation has shown that the core can be approximated by a straight line which extends from the apex to the trailing edge and then turns toward the freestream direction.

In accordance with the treatment of the Kutta condition, these boxes have the same doublet strength as the leading-edge box they abut. In a strict sense, since the vortices do not leave the edge in the streamwise direction, the Kutta condition was enforced at neither the leading edge nor the trailing edge, where the attached-flow model's wake was retained.

However, the numerical model had enough latitude with respect to the application of the Kutta condition that even gross approximations concerning the flow as it leaves the leading and trailing edges yielded acceptable pressure distribution near the edge.

The computational procedure is:

1. Input  $AR, \alpha, X_V, Y_V, Z_V$
2. Calculate  $[C_w]$
3. Calculate  $\{w_x\}$
4. Solve Equation 15b for  $\{K\}$
5. Calculate  $[C_u]$  and  $[C_v]$
6. Find:  $\{u\} = 1/4\pi [C_u] \cdot K$ ;  $\{v\} = 1/4\pi [C_v] \cdot K$
7. Calculate the pressure distribution over the wing using Equation 18e

Results obtained with this model indicated its limitations are the same as those of the analytic theory of Brown and Michael, making it applicable only to low aspect ratio wings. For an aspect ratio of one, the predicted  $C_L$  versus  $\alpha$  curve is very close to experimental curves (see Figure 14). This agreement drops off rapidly with increasing aspect ratio, indicating a practical limit for the model of  $AR = 1.5$ .

Because the trailing-edge Kutta condition was not strictly enforced, the center of pressure was not as far forward as the experimental position. As Figure 15 shows, the center of pressure was just forward of the centroid of the wing which is the center of pressure predicted by slender wing theory. Interestingly, wings with practical thicknesses have centers of pressure closer to those predicted by the lifting-surface theory than very thin wings.

The computed pressure distribution bears a strong resemblance to experimental results as illustrated in Figure 16. This figure, showing the spanwise pressure distribution near the center of pressure (65% root chord), indicates good agreement between the computed and measured values of the centerline loading coefficient ( $\Delta C_p$ ) and the peak  $\Delta C_p$ . Because the analytic results of Brown and Michael predict a vortex core on location outboard of experimental positions, the suction peak computed here also lies outboard of the observed peak. Secondary separation will also contribute to the slight discrepancy between the two curves since it puts a depression on the outboard side of the suction peak.

The value of the fixed-wake model lies in its simplicity. The required input can be fitted on one card, and no time-consuming iteration is needed. In fact, the run times were less than 5 seconds (including WATFIV compilation) on the Amdahl 470V/6.

Some thought has been given to improving the fixed-wake model. It is believed that the use of more realistic vortex core locations would move the peak suction inboard with subsequent closer agreement with experiment. The aspect-ratio range for which the program is accurate might be extended by adjusting the angle at which the feeder vortices leave the leading edge, because the lift coefficient in the free-wake model was found to be very sensitive to this angle. This adjustment could use another angle for all aspect ratios or an angle which is a function of aspect ratio.

#### Free-Wake Model

Essentially, the representation of the leading-edge vortex sheet in the free-wake model is by means of discrete vortices attached to the leading edge. These vortices are allowed to align themselves with streamlines to

meet the wake criteria of tangent flow and of being a free surface. These discrete vortices are formed by the boundaries of the semi-infinite subregions into which the vortex sheet is divided. The vortices are described by line segments whose endpoints are specified in vertical planes which coincide with the spanwise lines that bound the vortex boxes on the wing surface (figure 17). Beyond the trailing edge of the wing, the vortices are straight lines trailing straight back.

In this model, the trailing wake was also free to a certain extent to align itself with streamlines. Instead of being a straight line trailing aft, as in the attached-flow model, the vortices in this trailing-edge wake consisted of a short line segment attached to the trailing edge and then a semi-infinite trailer. These short segments extended a distance of 10% of the root chord aft of the trailing edge, and together with the trailer were inclined vertically as in the attached-flow model (Figure 18). Within this inclined plane, though, the short segments were aligned in the direction of the streamlines leaving the trailing edge. Numerically, no problems resulted from this representation, although in some cases the short segments intersected, which is physically impossible.

In the computer program the doublet strength ( $K$ ) distribution was not obtained directly through Equation 15b. Rather, the aerodynamic influence matrix was broken up into three matrices representing the contributions of the wing, leading-edge sheet, and trailing-edge wake. Equation 15b was rewritten:

$$[C_w]_w \{K\}_w = -4\pi \{w_\infty\} - [C_w]_V \{K\}_V - [C_w]_{TE} \{K\}_{TE} \quad (23)$$

The matrix subscripts refer to the wing ( $w$ ), leading-edge vortex sheet ( $V$ ),

and trailing-edge wake (TE). In this form the wing-on-wing influence matrix,  $[C_W]_W$ , which does not change with each iteration and which is the largest matrix, need only be calculated once. This matrix can then be decomposed by the Cholesky matrix solution method allowing repeated, rapid calculation of  $\{K\}_W$  for each different right-hand side that occurs every time the wake geometry is changed. The right-hand side calculations are performed using the assumed geometries and strengths for the leading-edge and trailing-edge wakes.

To improve the assumed geometry of the wakes the velocities at the endpoints of the segments forming the wake vortices are calculated from the free stream and the induced velocities, i.e.,

$$4\pi \{V\} = 4\pi \{V_\infty\} + [C]_W \{K\}_W + [C]_V \{K\}_V + [C]_{TE} \{K\}_{TE} \quad (24)$$

These velocities are then used to improve the shape of the wake, so that the vortices more closely follow streamlines. It should be noted that the aerodynamic influence matrices in Equation 24 refer to the influence of the lifting-surface on the points in the leading-edge sheet. The matrices in Equation 23 refer to the influence of the lifting-surface on the wing. These matrices are not the same.

Originally, the updating of the vortex positions in the leading-edge sheet was dependent on the Cartesian velocities (u,v,w). However, for points near the apex or close to the vortex core the curvature of the spiral sheet becomes so severe that the Cartesian velocities are useless in predicting the streamlines for any practical grid fineness.

A great deal of this difficulty is overcome by adopting the polar coordinate system, shown in Figure 19, which is consistent with the

experimentally known shape of the vortex sheet. The  $v$  and  $w$  Cartesian velocities are transformed to tangential and radial velocities with respect to the position of the vortex core. The variation of the polar velocities along a vortex is much smoother than the variation of the Cartesian velocities, which indicates that this coordinate system is more natural for predicting the vortex geometry.

Referring to Figure 20, the new angular and radial coordinates of the downstream end of a segment are predicted with these equations:

$$\theta_2 - \theta_1 = \left( \frac{d\theta}{dx} \right)_{\text{avg}} \Delta x = \frac{1}{2} \left( \frac{u_{\theta_1}}{R_1 u_1} + \frac{u_{\theta_2}}{R_2 u_2} \right) \Delta x \quad (25)$$

$$R_2 - R_1 = \left( \frac{dR}{dx} \right)_{\text{avg}} \Delta x = \frac{1}{2} \left( \frac{u_{R_1}}{u_1} + \frac{u_{R_2}}{u_2} \right) \Delta x \quad (26)$$

In this way the change in the angular and radial coordinates between any two chord stations is approximated by the average rate of change of each coordinate multiplied by the chordwise distance.

Unfortunately, this coordinate system does not completely solve the problem of increasing curvature near the vortex core. This problem is compounded by the poor prediction of the velocities near the vortex core which is inherent in discrete vortex representations. Consequently, the sheet near the center is poorly reproduced and the positions of the vortices sometimes indicate an unrealistic intersection of the sheet upon itself.

To circumvent these problems a finite-sized vortex core was defined as in Figure 21. In the program two circles centered about the vortex

core limit the extent of the vortex sheet. The size of these circles grow continuously downstream of the apex so that the ratios of circle radii to local wing semi-span is constant. If the endpoint of a segment is predicted to lie inside the inner circle, the segment's endpoint is moved to the center. This capture is reversible. If the upstream end of a segment (whose downstream end is captured) lies outside the outer circle, the position of its downstream end will be approximated such that the downstream end can escape the core. Additionally, to prevent the sheet from intersecting itself, a maximum allowable angle is specified, as also illustrated in Figure 21. If a vortex exceeds this angle it will be moved to the center.

This core model resembles that of Mangler and Smith<sup>5</sup>, who showed that the effect of the core of the spiral sheet on the field outside was equivalent to a concentrated vortex at the center of the core. Smith<sup>6</sup> later refined their work including the specification of a maximum sheet extent angle and evaluated the effect of this parameter.

It is interesting to note that if the core is given a large enough radius the result will be a model similar to the Brown and Michael model.

No criteria have been developed here to predict the position of the vortex core due to the inaccuracy of predicting its velocity. Rather than iterate on the position of the core, the analytical predictions of Smith<sup>6</sup> were used for the positions of the core (Figure 22). His conical flow assumption is followed in the model to the trailing edge, and then the core is assumed to trail straight back with a slight incline, as in the fixed-wake model.

The computational procedure for the free-wake model is:

1. Input  $AR$ ,  $\alpha$ ,  $Y_V$ ,  $Z_V$ , Assumed leading-edge vortex strength and geometry, Assumed trailing-edge wake strength and geometry

2. Calculate and decompose the wing-on-wing influence matrix
3. Calculate vortex- and wake-on-wing influence matrices
4. Calculate right-hand side of Equation 23
5. Obtain wing doublet distribution
6. Update L.E. vortex and T.E. wake strengths
7. Update L.E. vortex and T.E. wake positions  
(iterate between 3 and 7 until convergence)
8. Calculate pressure distribution over the wing

Some exploratory cases run as described indicated that a few modifications should be made. The first modification was prompted by the observation that, when one of the free vortices was of odd sign in strength, geometry predictions were poor to the point of being unstable. The solution was to fit the strengths of the strips on the leading edge sheet,  $\{K\}_V$ , to a polynomial curve. By forcing these strengths to fit a curve of low enough order all the vortices retained the same sign. In fact, for a fourth order curve, the vortices were all of the same sign; and yet when a converged case was obtained, the leading-edge boxes and attached wake strips differed negligibly in strength, implying that the Kutta condition was still being satisfied. A second purpose which this curve fit served was insuring the doublet strength at the apex was zero.

The second change concerned the vortices as they leave the leading edge. The point at which these vortices originate is on the leading edge where the induced velocities cannot be accurately calculated. If the tangent off-flow condition is arbitrarily enforced, that is, the net velocity at the leading edge set to zero, the lift coefficient will change by approximately 30 percent. This sensitivity is due to the proximity of

the leading-edge collocation points to the vortices leaving the leading edge and has been noted by other analytic and numerical sources.

The modification was to break the first segment of each vortex into two segments with the break occurring at 20% of the original segment's length (Figure 23). By breaking the segment very close to the leading edge, another point is established at which the velocities can be calculated accurately, which leads to more accurate predictions of the sheet geometry in this critical region.

Convergence. To date, no objective basis has been established for determining when the program has converged to a solution. The possibility of unrealistic vortex geometries being generated still dictates that a programmer evaluate the program's progress every five to ten iterations, as opposed to approximately twenty-five iterations required for convergence. Such being the case, it has been left to the programmer to determine convergence. This determination is done through comparison of vortex geometries and lift coefficients, while another accurate indicator is the doublet strength at the wing tip. Regardless, judging from the experience of having run the cases presented here, further iteration should vary the  $C_L$  by no more than 5 percent.

An average case required five runs, each run updating the geometry of the leading-edge vortex sheet five times. The total run time of 75 seconds CPU time (on the Amdahl) can be reduced, since each separate run requires decomposition of the wing-on-wing influence matrix. Another factor affecting computational time is the initial approximation to the sheet geometry. Here, results were first obtained at  $\alpha = 20^\circ$  for aspect ratios of one and two, using hand-drawn spirals as first approximations.

Then the converged geometries of these cases were used as first approximations at  $\alpha = 15^\circ$ , etc.

Results. The results, as presented in Figures 24 through 28, are encouraging. At an aspect ratio of one, the vortex lift is over predicted (Figure 24), but the general trend of increasing lift-slope with angle of attack is followed. At aspect ratio two (Figure 25), the comparison with experiment is much better. The difference between the data and the prediction is within the uncertainty band of the data.

With a better model of the trailing edge the center of pressure (Figure 26) has moved forward compared to the fixed-wake model (Figure 15, p. 30). The free-wake prediction now agrees more closely, especially in trend, with the thick wing position, but still does not show the thin wing's far forward position.

A carpet plot of the loading coefficient, Figure 27, shows the predicted distribution follows the peak and valley form of experimental measurement. Again, as in the fixed-wake model, the loading along the centerline is predicted well, but the suction peak is lower and further outboard of experiment. This discrepancy between the positions of the suction peaks may be due to the edge shape of this particular wind-tunnel model, since this shape has a noted effect on the core position.

Near the trailing edge, the experimental data shows a loss of vortex suction, the reason for the forward position of the center of pressure in thin delta wings. This loss of suction seems to be associated with the position of the vortex core. As it nears the trailing edge the core passes out of the conical flow region and starts to parallel the freestream. Consequently, its height above the trailing edge is greater than that predicted by conical flow, and its influence is therefore less.

Smith's<sup>6</sup> theory for predicting the core position should not be overlooked as a source of inaccuracy in the pressure distribution. His core positions are also known to be slightly outboard of reported data. Nevertheless, some aspects of the theory are borne out by experimental observation and numerical check. For example, conical flow predicts the same leading-edge sheet geometry for a unit aspect ratio wing at  $\alpha = 10^\circ$  as it does for an aspect ratio two wing at  $20^\circ$ . Using a fixed sheet geometry predicted by the program for AR - 2,  $\alpha = 20^\circ$ , the unit aspect ratio pressure distribution was computed. The lift coefficient obtained this way varied by less than 5% from the free-wake case; but, the error in the theoretical position of the core seems the most likely cause for the over prediction of the vortex lift on the aspect ratio one wing. If this is so, a simple, fixed-wake model based on the geometries predicted by the free-wake model will be difficult to achieve without using conical flow.

Figure 28 shows one example of the predicted geometry. The spiral reflects more of the experimentally observed roll-up than the results of Kandil et. al.<sup>10</sup> or Rehbach.<sup>11</sup> A disadvantage of the discrete vortex scheme is also shown. Beneath the core the spanwise velocities are so high that no more than one vortex is ever present between the core and the wing. Thus, the sheet in this area is not well represented; which may be the cause of suction peaks lower than observed.

Future Improvements. The free-wake model must be modified, though, if it is to be useful for higher aspect ratio wings. It appears that for aspect ratios of three and higher the calculations for vortex segment position become incorrect. At these aspect ratios the u velocity beneath the core becomes negative. The equations (25, 26) for predicting the position of the segments implicitly assume positive u velocities and, hence,

they fail at higher aspect ratios. A new coordinate system using the vortex core as one axis and radial and angular coordinates similar to those described will probably be adopted. The velocity along the core is known to be greater than the freestream which will alleviate the problem of negative  $u$  velocities.

At the same time it would be advantageous to modify the grid on the wing, since at low values of  $\underline{a}$ , ( $\alpha/\tan \epsilon$ ), the wing doublet strength beneath the core has a very high gradient. Such gradients are contradictory to the assumption that  $K$  may be considered constant in each panel on the wing. Therefore, a fine grid should be imposed on the wing beneath the core, which would also assist in calculating the loading in this critical area.

A more sophisticated predictor will allow the program to reach convergence without operator help. This will improve run times; but it will require the adoption of convergence criteria. The use of convergence criteria will also be advantageous since the introduction of objectivity could improve the consistency of the program.

Finally, the vortex core should be positioned on a basis other than conical flow theory. Experimental results might be used, but ultimately a numerical prediction will be made.

#### Conclusions

A general potential flow theory, including the effects of leading-edge separation, has been presented and applied specifically to delta wings. Two different models of the leading-edge separation were constructed numerically: a fixed-wake model, and a more refined free-wake model.

The fixed-wake model is simple, fast, and accurate for low aspect ratio wings, but it does not provide detailed information about the flow.

The free-wake model has a larger aspect ratio range for which comparatively accurate answers can be obtained. It also provides some qualitative results on the shape of the leading-edge vortex sheet. Its disadvantages are longer computational times and the need for operator supervision.

Methods of enlarging the range of aspect ratios for which the models are valid have been proposed. Some of these are now being evaluated and will be incorporated into a generalized program combining the fixed-wake and free-wake concepts.

## II. EXPERIMENTAL INVESTIGATION

### Equipment and Tests

Most of the work on delta wings in unsteady flow has been done by moving wings in a steady flow<sup>(38-42)</sup>. Whilst the basic mechanics of this approach are straightforward it does lead to problems with data acquisition and recording and might not be representative of an aircraft entering a gust. In particular, the thin wing used in these tests was subject to unacceptable flexure when pitched rapidly. Therefore, the reverse approach of statically mounting the wing in a variable airstream was pursued.

For the current tests, a thin sharp-edged delta wing,  $AR = 2$ , was mounted in the Texas A&M University 7' x 10' Low Speed Wind Tunnel (Fig. 29) and a stream oscillation device<sup>(43-44)</sup> (Fig. 30) used to produce a sinusoidal variation in flow angle of the airstream. The system uses two flapped vanes at the entrance to the test section, the sides of which have been removed. The flaps are oscillated by a variable speed electric motor and produce a sinusoidally oscillating airstream, of constant amplitude, in the test section.

Frequencies of oscillation of 2Hz and 4Hz were used and in conjunction with an airspeed of 83.8 ft./sec resulted in reduced frequency parameters,  $k$ , of 0.2 and 0.4 at a Reynolds number of  $1.3 \times 10^6$ . With these frequencies and tunnel speed the total wavelengths of the flow were 42 ft and 21 ft as compared to the root chord length of 4 ft for the delta wing. The flow angle amplitude chosen for the tests was  $\pm 8^\circ$  about a mean angle of attack of  $15^\circ$ .

The tests were divided into two sections, flow visualization and pressure measurements. For the flow visualization a liquid nitrogen and steam smoke generator developed at Texas A&M<sup>(45)</sup> was used to seed the vortex cores. Initially the position of the vortex core and burst point (if it occurred)

in steady flow were determined at  $5^{\circ}$ ,  $10^{\circ}$ ,  $15^{\circ}$ ,  $20^{\circ}$ ,  $25^{\circ}$ ,  $30^{\circ}$  angle of attack, by photography (Fig. 31). In the unsteady case photographs of the vortex locations at a particular point in a cycle were obtained using strobe lights, slaved off the flap drive motor, to illuminate the flow (Figs. 32-34) the rest of the tunnel being darkened. The loci of the vortex burst point versus angle of attack were determined from these photographs (Fig. 35). For detailed chronological analyses, the two unsteady tests were filmed using high-speed cameras operating at 200 frames per second. These films can be correlated with other data by a flap-motor indicator (reflected by a mirror) in the camera's view.

For the pressure measurements twenty Validyne DP9 pressure transducers were mounted on the wing with one side of each transducer connected to a port on the upper surface (Fig. 36) while the other side was connected to a plenum referenced to free-stream static pressure. Outputs from all transducers, together with a signal indicating the flap position were recorded on Honeywell visicorders. Again results were obtained for both steady and unsteady flow. After reduction the load distributions on the wing were plotted at several angles of attack throughout a typical cycle at each frequency (Fig. 37).

## Discussion

### 1) Flow Visualization

#### a) Steady Flow

At  $5^{\circ}$  angle of attack in steady flow (Fig. 31) the vortices above the wing are weak and it proved impossible to seed the cores adequately with smoke. When  $\alpha$  is increased to  $10^{\circ}$  the vortex core is well defined and easily seeded, towards the trailing edge the core tends to curve

into the stream direction. Increasing  $\alpha$  to  $15^\circ$  causes the burst to move up to the trailing edge in the lower vortex, no bursting being evident in the upper vortex. The slight asymmetry is probably due to either a small yaw angle on the wing or a disturbance to the flow caused by the smoke probe.

At  $20^\circ$  angle of attack, the vortices have moved further inboard and the burst point has moved forward to almost 50% of the root chord. These trends continue until at  $\alpha = 30^\circ$  the burst point has moved forward to almost the 20% root chord position.

The position of the burst point as a function of angle of attack is plotted in Figure 35 and as can be seen the burst point moves steadily forward with increasing angle. The points at which the core begins to burst and when the smoke is no longer visible are plotted to indicate the severity of the burst. Numerically, the results are consistent with Lambourne's, at all angles of attack the burst point in these tests lies slightly ahead of Lambourne's<sup>33</sup> measurements as one would expect for a slightly larger aspect ratio (2.0 as opposed to 1.86).

In the current steady flow tests, the burst was always of the axisymmetric "tulip" type (this was also true for some preliminary tests at  $R_N = 3 \times 10^5$ ). According to Sarpkaya<sup>18</sup> the spiral type of vortex breakdown is more commonly observed over delta wings and Maltby et al.<sup>42</sup> were able to produce a spiral burst over an aspect ratio one wing in a wind tunnel at Reynolds numbers of  $1.5$  and  $6 \times 10^6$ . However the observations reported here are consistent with the results of Lambourne who pointed out that his observations of the spiral type of burst were at very low Reynolds numbers in a water tunnel.

#### b) Oscillatory Flow

The analysis of the unsteady flow is based on the still photos presented

in Figures 32 and 33 and the high speed films. The angle of attack is referred to the instantaneous angle of attack at the aerodynamic center ( $\alpha_{2/3C_R} = 15^\circ + 8^\circ \sin \omega t$ ).

The still photos of the flow at 2Hz (Fig. 32) indicate that at  $15.3^\circ$  with the angle of attack increasing the vortex is still fairly weak and no burst occurs above the wing. When the angle has increased to  $20.9^\circ$  the vortex has moved inboard and bursts at about the 60% root chord point. It should be noted however that this burst does not appear to be of the same type as that observed in steady flow (Fig. 31), the burst does not have the classic 'tulip' shaped bubble normally seen with an axisymmetric burst. Rather the core seems to expand gradually, become turbulent and dissipate. By the time the maximum angle of attack has been reached  $23^\circ$  the burst point has moved forward but still appears to be of a gradual diffusion type. At  $20.5^\circ$  and decreasing the burst point has not changed location but its character has changed. This trend continues until  $\alpha = 14.7^\circ$  when the burst has moved downstream and become a helical type burst (see also Fig. 34) where the core has an abrupt kink and then swirls around its axis before dissipating into turbulence. The whole process is much more rapid than the gradual increase of core size previously described. By  $9.1^\circ$  angle of attack the burst point is near the trailing edge of the wing and the vortex is decreasing in strength. As the angle passes through a minimum the burst moves off the wing and the core moves outboard before moving inboard again with increasing angle ( $\alpha = 9.5^\circ$ ).

The point of the burst for  $k = 0.2$  significantly lags the position in steady flow, also the burst point in oscillatory flow never moves as forward on the wing as it does in steady flow. This is presumably because it takes a finite time for the vortex strength to increase after the leading edge shedding rate has changed due to angle of attack increase, it will then take

a further period of time for the instabilities to cause the burst point to move forward. By this time the angle of attack has decreased and the shedding rate changed, i.e. the wing is not at the maximum angle of attack long enough for the steady state conditions to occur, the integrated vortex strength which must affect the burst location is always less in unsteady flow than it is at the maximum angle of attack in steady flow.

Figure 38 produced from data taken from the high speed film presents graphically the position and character of the burst. Firstly, it should be noted that the vortex core was not seeded well enough to allow plotting of the burst during the increasing part of the cycle. Up to the maximum angle the diffuse core focuses until the beginning and end of the burst can be determined with some certainty. At  $23^{\circ}$  the core begins bursting at 60% of the root chord. The initial burst point moves only slightly forward while the terminal end of the burst moves rapidly forward as the burst changes from gradual diffusion to a helical burst. As the angle of attack decreases from  $17.5^{\circ}$  the burst moves rearward until the core is too weak to appear.

For  $k = 0.4$  (Fig. 33) the trends are similar to those observed at  $k = 0.2$ . At  $17.3^{\circ}$  with the angle of attack increasing there is no burst above the wing. As the angle increases to just above  $20^{\circ}$  the burst moves onto the wing and by  $22.1^{\circ}$  it occurs at about the 60% chord location. Determination of the exact burst point at this angle is extremely difficult because of the very gradual expansion of the core into turbulence. Just after the maximum angle has been reached ( $\alpha = 22.7$ ) the burst point is much better defined but is still axisymmetric in nature. As the angle decreases

through  $18.8^\circ$ ,  $12.7^\circ$  and  $7.9^\circ$  the burst changes character becoming helical and moving downstream. The burst point moves off the wing as the minimum angle of attack is reached.

Figure 39 is similar to Figure 38 but the diffuse phase of the vortex is much more exaggerated. Again, the determination of the initial and terminal burst points is difficult near the maximum angle. Presumably the effective angle at the apex increases quickly enough that the initial burst does not propagate upstream but is reformed each cycle and moves rearward with decreasing angle of attack.

## 2) Pressure Measurements

All the pressure data obtained, both steady and unsteady, is presented in the form of carpet plots at several angles of attack in Fig. 37.

With the wing at  $15^\circ$  angle of attack in steady flow (Fig. 37a) the two suction peaks, near the nose are narrow and close to the leading edges, further downstream the peaks move slightly inboard, spread out and decrease in magnitude due to the effects of secondary separation and the Kutta condition of the trailing edge. In unsteady flow the distribution is similar but the peaks are slightly lower for  $k = 0.2$  and lower still for the  $k = 0.4$  case. This trend continues up through  $\alpha = 17.5^\circ$  (Fig. 37b - Note steady flow data was only obtained at  $5^\circ$  intervals) with the suction peaks being higher at  $k = 0.2$  than at  $k = 0.4$ .

At  $\alpha = 20^\circ$  (Fig. 37c) these trends are still true at the most forward measuring station ( $x/c_R = 0.4$ ) but at the midstation ( $x/c_R = 0.6$ ) the peaks in unsteady flow are slightly greater than in steady flow. The reason for this is probably in the vortex burst, in steady flow the burst occurs

ahead of whilst in unsteady flow it has not yet reached, this location, thus in unsteady flow full vortex suction is still being maintained. Peaks for  $k = 0.2$  are slightly higher than for  $k = 0.4$ . At the rear station the peaks for  $k = 0.2$  and  $0.4$  are about the same magnitude as the vortex has burst upstream of this location at  $k = 0.2$  but has not for  $k = 0.4$ , thus the loss of suction due to bursting cancels the loss due to phase lag.

By the time maximum angle of attack ( $23^\circ$  Fig. 37d) has been reached the vortex burst has moved ahead of  $x/c_R = 0.6$  for both frequency parameters and distributions of  $x/c_R = 0.6$  and  $0.8$  look similar for both cases. The suction peaks at  $x/c_R = 0.4$ , where no burst occurs in either case, are greater for the lower frequency.

By comparing the distributions at the various angles of attack it can be seen that the total load on the wing increases steadily as the angle of attack increases from  $15^\circ$  to  $23^\circ$ .

When  $\alpha$  decreases to  $20^\circ$  (Fig. 37e) the loading for all cases is similar, and might be expected since this is the angle at which the burst patterns are in phase. A major difference between the steady and unsteady data is that the dips due to secondary separation apparent in the steady data are not present in the unsteady distributions, this might just be due to the ports being located at the 'wrong' places to measure secondary separation in unsteady flow. At the most forward station the peaks for  $k = 0.2$  lie slightly outboard and are slightly lower than the steady or  $k = 0.4$  results. The distribution changed little between  $23^\circ$  and  $20^\circ$ .

Again little change in loading occurs as the angle of attack further decreases to  $17.5^\circ$  (Fig. 37f) but as the angle decreases to  $15^\circ$  (Fig. 37g)

the load on the wing begins to decrease. An interesting point at this angle is the distributions of  $x/c_R = 0.6$  and  $0.8$ , the suction peaks in unsteady flow are quite broad whilst they are sharp and narrow for steady flow. In steady flow at this angle vortex bursting does not occur until the trailing edge whilst at  $k = 0.2$  it occurs at about  $x/c_R = 0.6$  and somewhat further forward for  $k = 0.4$  causing the peaks to become broader and lower. A similar phenomena occurs at  $\alpha = 12.5^\circ$  (Fig. 37h) where the peaks at  $x/c_R = 0.6$  and  $0.8$  are broader and lower for the higher frequency.

As  $\alpha$  decreases to  $10^\circ$  (Fig. 37i) the total lift continues to decrease. The vortex loading in unsteady flow at the two forward stations is considerably greater than for steady flow. At the rear station vortex burst causes the peaks to broaden and decrease in magnitude for unsteady flow.

At the minimum angle of attack,  $\alpha = 7^\circ$  (Fig. 37j), the vortex peaks at  $x/c_R = 0.4$  for  $k = 0.2$  have become very narrow and have not moved as far outboard as have the peaks for  $k = 0.4$ . The reason for this is not known but it might be connected with the rapid collapse of the vortex core at low angles in large amplitude oscillatory flow as discussed by Lowson<sup>39</sup>.

As the angle of attack increases back up to  $10^\circ$  (Fig. 37k) the lift continues to decrease. It is not until  $12.5^\circ$  (Fig. 37l) that the lift starts to increase again with increasing magnitudes of vortex suction.

In general it can be seen that in oscillatory flow there is a phase lag, that increases with frequency, in the development of vortex lift. This is not so in the loading away from the influence of the vortices i.e. along the center of the wing. Flow that comes over the vortices and reattaches along the centerline of the wing (the 'potential' flow) responds fast enough that there are no phase lags within the accuracy of measurement (except at

high angles where the center section is influenced by the vortices). The phase lag that occurs in the vortex loading must occur because of the finite time it takes the vortex strength to change after a change in the leading edge shedding rate, this is consistent with the measured lags in the locus of the burst points.

In the results presented here no wind tunnel boundary corrections have been applied. Estimates for the magnitude of the angle of attack correction were made using standard steady flow vortices of lift coefficient and these indicated that at  $\alpha = 7^\circ$  and  $23^\circ$  correction of order  $-0.2^\circ$  and  $-0.6^\circ$  would be needed. However this type of corrections cannot be rigorously justified in unsteady flow and so none have been applied.

#### Conclusions

In steady flow at Reynolds numbers of order  $1 \times 10^6$ , a delta wing of  $AR = 2$  the vortex bursting that occurs is of the axisymmetric 'tulip' type and the burst point moves upstream with increasing angle of attack. In unsteady flow ( $\alpha = 15^\circ + 8 \sin \omega t$ ) this type of burst does not occur. As the angle of attack increases the vortex core appears to undergo a gradual viscous dissipation into turbulence whilst with decreasing angle a helical (i.e. the vortex core swirls about its own axis) burst was observed. The locus of the burst point in unsteady flow lags the steady position over most of the cycle. The burst point does not move as far forward in unsteady as it does in steady flow, probably because the vortex strength takes a finite time to build up and the leading edge vorticity shedding rate is not maintained at the maximum value long enough for the vortex to reach equilibrium.

Measured pressure distributions indicate that the suction pressures due to the vortices in unsteady flow lag behind the steady state pressures through most of the cycle whilst the loading in regions of 'potential' flow remain in phase with the angle of attack variation confirming that the vortices take a finite time to change strength after a change in angle of attack. Vortex bursting decreases the suction pressure and broadens the peak causing a decrease in lift downstream of the burst. When the angle of attack is decreasing the locus of vortex bursting lags the steady state position by large amounts causing a significant loss of lift over the rear of the wing to much lower angles of attack than might be anticipated from steady flow data.

## REFERENCES

1. Bergeson, A.J. and Porter, J.D., "An Investigation of the Flow around Slender Delta Wings with Leading-Edge Separation", Princeton Rpt. 510, 1960.
2. Jones, R.T., "Properties of Low Aspect Ratio Pointed Wings at Speeds Above and Below the Speed of Sound", NACA Report 835, 1946.
3. Legendre, R., "La condition de Joukowski en ecoulement tri-dimensionnel", Recherche Aerospatiale, No. 5, pp. 241-248, 1952.
4. Brown, C.E. and Michael, W.H., "On Slender Delta Wings with Leading-Edge Separation", NACA TN-3430, 1955.
5. Mangler, K.W. and Smith, J.H.B., "A Theory of Flow Past a Slender Delta Wing with Leading-Edge Separation", Proc. Roy. Soc. London, Ser. A, 251, p. 200, 1959.
6. Smith, J.H.B., "Improved Calculations of Leading-Edge Separation from Slender, Thin, Delta Wings," Proc. Roy. Soc., London, Ser. A, 306, pp. 67-90, 1968.
7. Pullin, D.I., "A Method for Calculating Inviscid Separated Flow about Conical Slender Bodies", ARL/A14, Australian Defense Scientific Service, Report 140, May 1973.
8. Nangia, R. and Hancock, G.J., "A Theoretical Investigation for Delta Wings with Leading-Edge Separation at Low Speeds", ARC CP No. 1086, 1968.
9. Mook, D.T. and Maddox, S.A., "Extension of a Vortex-Lattice Method to Include the Effects of Leading-Edge Separation", JA, 11, pp. 127-28, Feb. 1974.
10. Kandil, O.A., Mook, D.T. and Nayfeh, A.H., "Nonlinear Prediction of Aerodynamic Loads on Lifting Surfaces", AIAA Paper No. 74-503, June 1974.
11. Rehbach, C., "Calculation of Flows around Zero Thickness Wings with Evolutive Sheets", NASA TT F-15, 183, 1973a.
12. Weber, J.A., Brune, G.W., Johnson, F.T., Lu, P. and Rubbert, P.E., "A Three-Dimensional Solution of Flows over Wings with Leading-Edge Vortex Separation", NASA SP-347, March 1975, pp. 1013-1032.
13. Polhamus, E.C., "A Concept of the Vortex Lift of Sharp-Edge Delta Wings Based on a Leading-Edge Suction Analogy", NASA TND-3767, 1966.
14. Matoi, T.K., "On the Development of a Unified Theory for Vortex Flow Phenomena for Aeronautical Applications", AD #A012399, April 1975.

31. Lambourne, N.C., and Bryer, D.W., "Some Measurements of the Positions of the Vortices for Sharp Edged Delta and Swept Back Wings", A.R.C. 19,953, 1958.
32. Wentz, W.H., Jr. and Kohlman, D.L., "Wind Tunnel Investigations of Vortex Breakdown on Slender Sharp Edged Wings", NASA CR 98737 Nov. 1968.
33. Lambourne, N.C., and Bryer, D.W., "The Bursting of Leading Edge Vortices Some Observations and Discussion", A.R.C., R & M 3282, 1962.
34. Sarpkaya, T., "An Experimental Investigation of the Vortex Breakdown Phenomena", United States Postgraduate School Report NPS 59SL0071A July 1970.
35. Werle, H., "Sur l' eclatement des tourbillons d'apex d'une aile delta aux faibles vitesses", La Recherche Aeronautique, pp. 23-30, No. 74, 1960.
36. Elle, B.J., "On the Breakdown at High Incidences of the Leading Edge Vortices on Delta Wings", Journal of the Royal Aeronautical Society, p. 491, Vol. 64, 1960.
37. Earnshaw, P.B. "Measurements of Vortex Breakdown Position at Low Speed on a Series of Sharp-Edged Symmetrical Models", R.A.E. Technical Report No. 6407, 1964.
38. Lambourne, N.C., Bryer, D.W., and Maybrey, J.F.M., "The Behavior of Leading Edge Vortices over a Delta Wing Following a Sudden Change of Incidence" ARC R & M No. 3645 March 1964.
39. Lowson, M.V., "The Separated Flows on Slender Wings in Unsteady Motion Communicated by Dr. J.P. Jones", A.R.C. 24, 118, 1963.
40. Randall, D.G., "Oscillating Slender Wings in the Presence of Leading Edge Separation", R.A.E. Structures Report 286, 1963.
41. Dore, B.D., "Calculations of the Transient Forces on Delta Wings", N.P.L. Aero Note 1033, 1965.
42. Maltby, R.L., Engler, P.B., and Keating, R.F.A., "Some Exploratory Measurements of Leading-Edge Vortex Positions on a Delta Wing Oscillating in Heave with G.F. Man", ARC 3410, 1965.
43. Bicknell, J. and Parker, A.G., "A Wind Tunnel Stream Oscillation Apparatus", Journal of Aircraft, Vol. 9, No. 6 June 1972 pp. 446-447.
44. Parker, A.G. and Bicknell, J., "Some Measurements on Dynamic Stall", Journal of Aircraft, Vol. 11, No. 7 July 1974, pp. 371-374.
45. Parker, A.G. and Brusse, J. C., "A New Smoke Generator For Flow Visualization in Low Speed Wind Tunnels", Texas A&M University TEES Report 3029-75-02, July 1975.

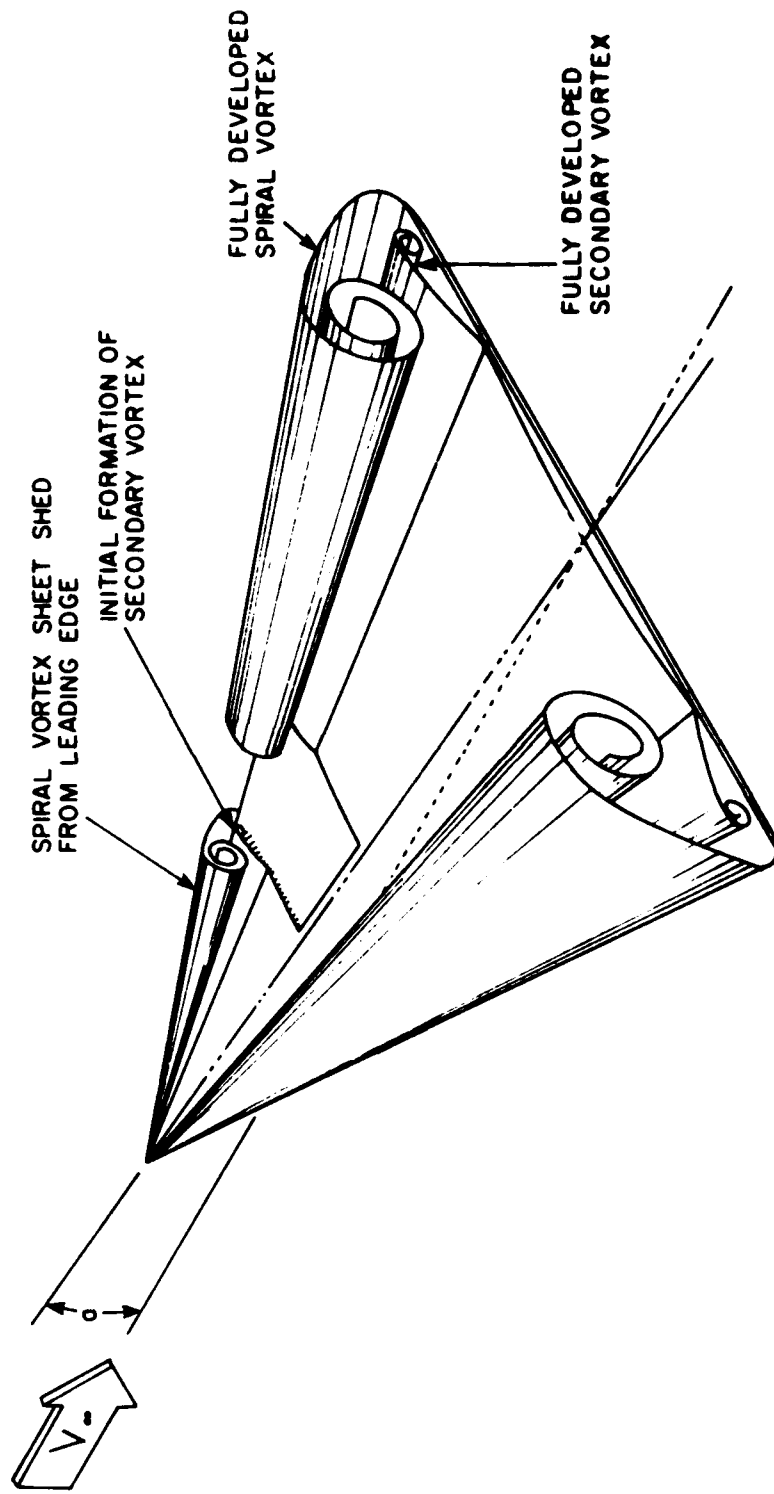


Fig. 1 FLOW OVER DELTA WING (Reference 1)

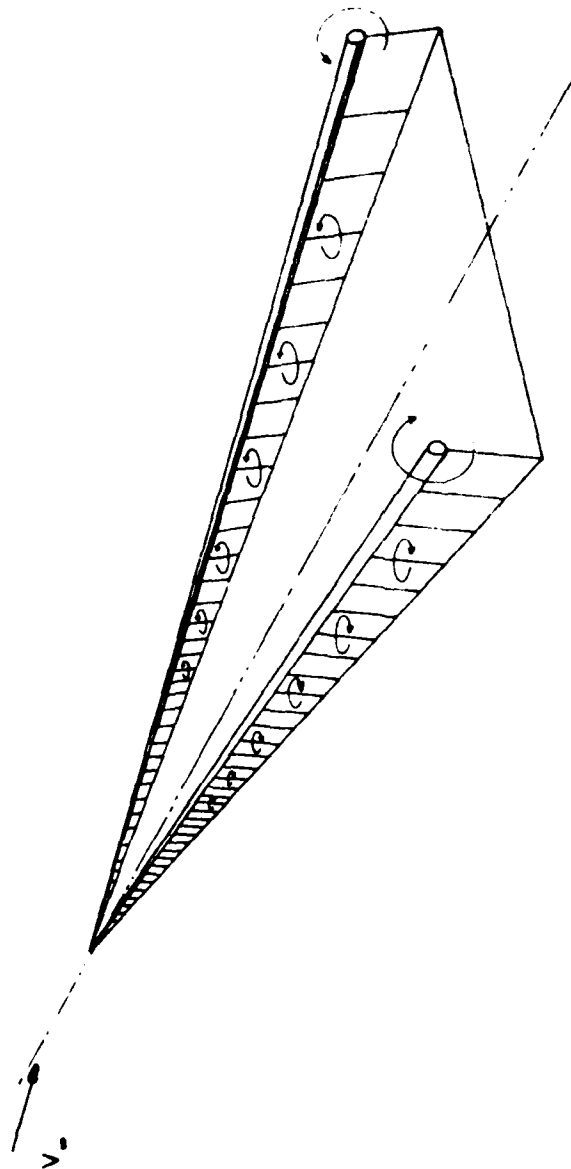


Fig. 2 MODEL OF BROWN AND MICHAEL



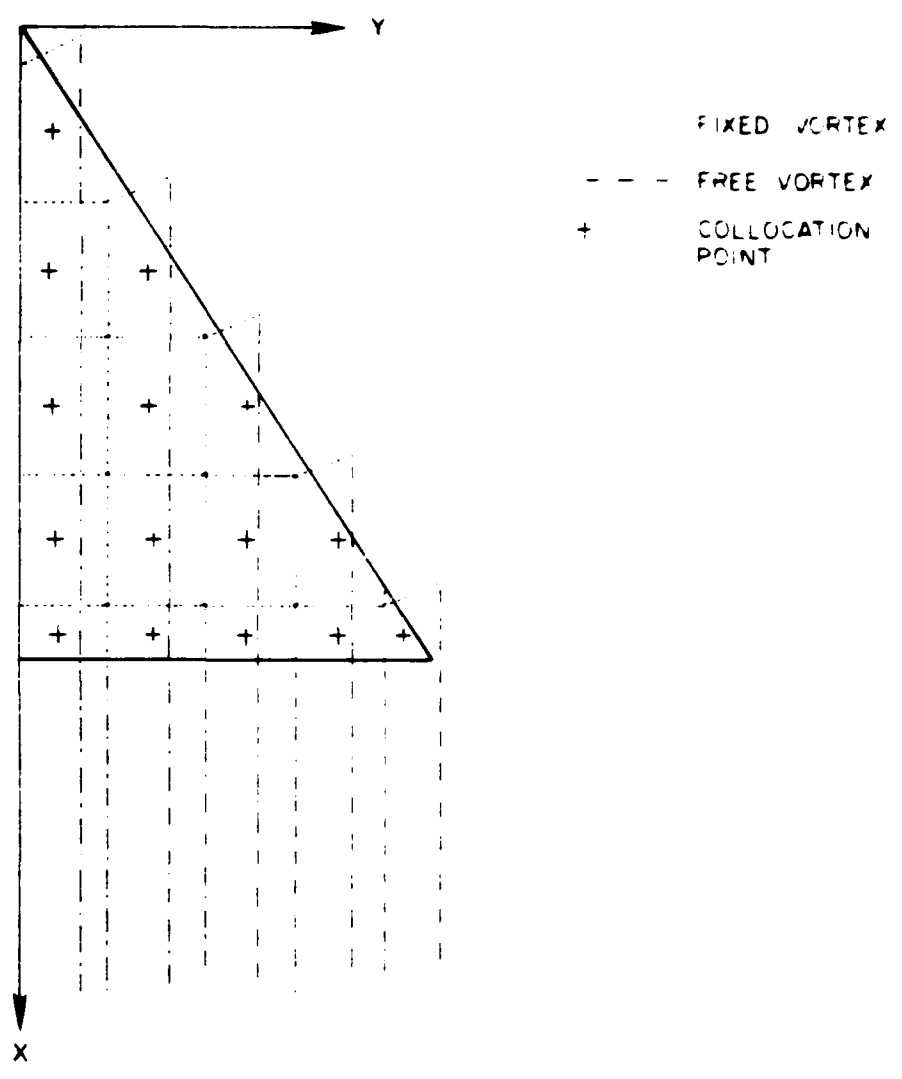


Fig. 4 VORTEX LATTICE OF KANEIL, MOON AND NAYFEH

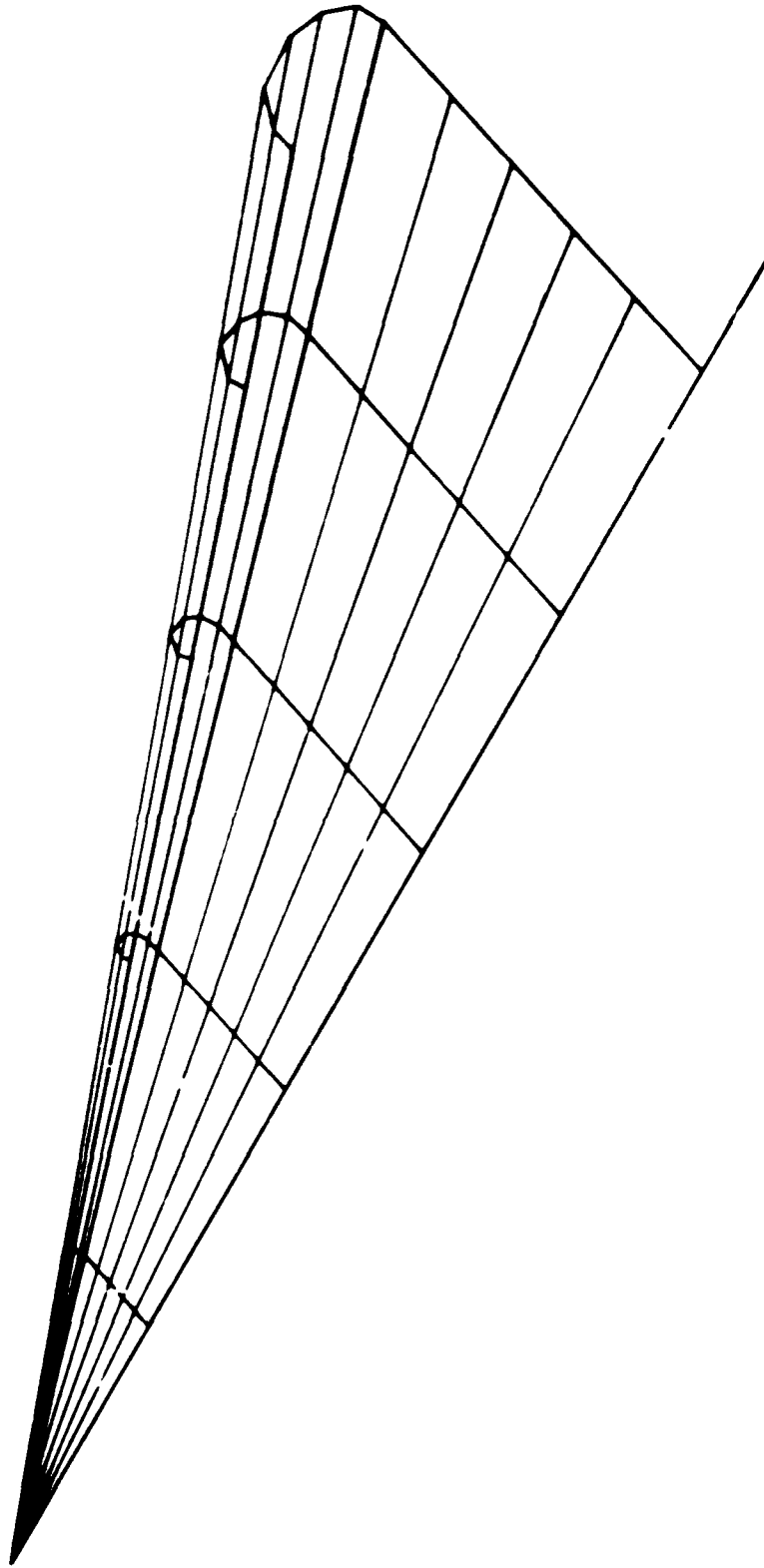
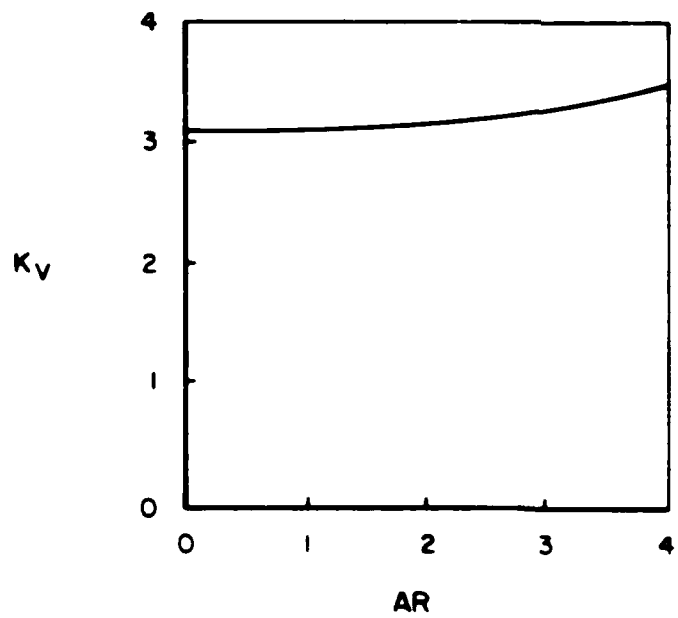
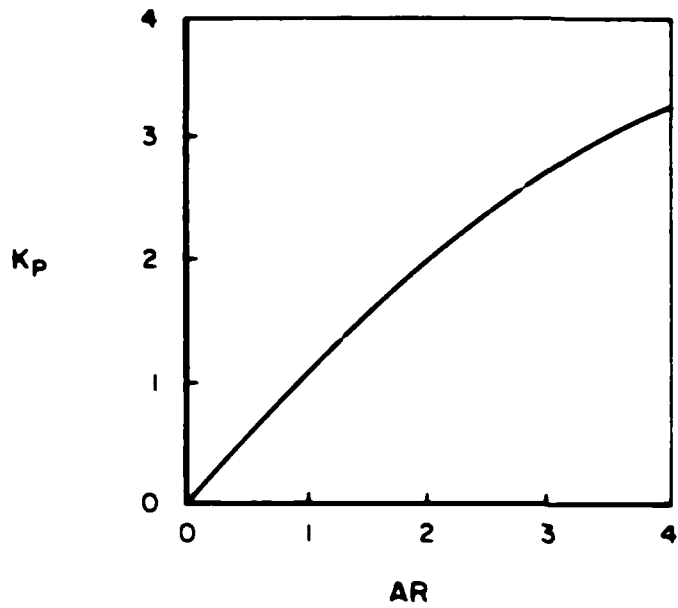


Fig. 5 PANEL MODEL OF WEBER



1. THE EFFECT OF INERTIA

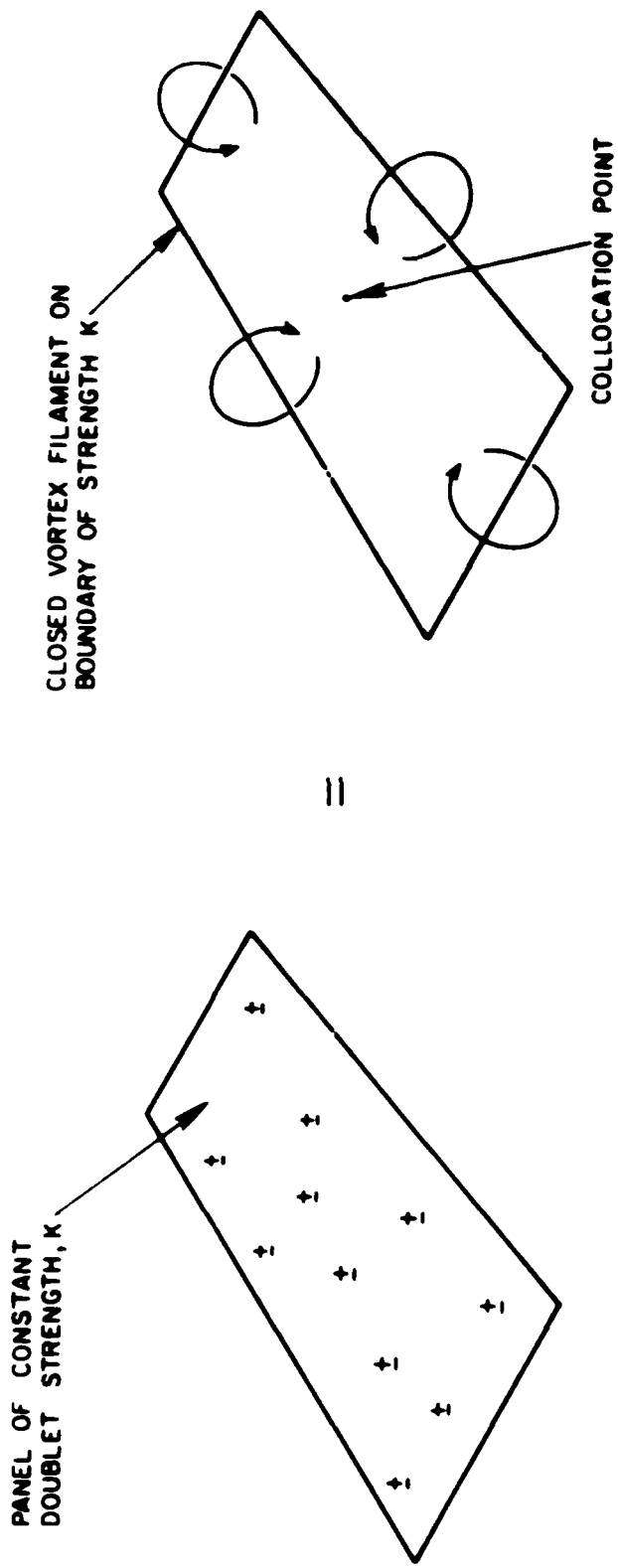


FIG. 7 EQUIVALENCE OF DOUBLET PANEL AND VORTEX BOX

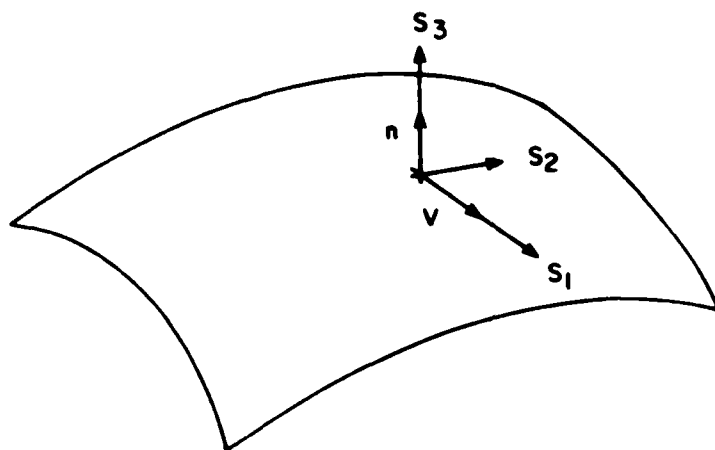


Fig. 8 VELOCITY ORIENTED COORDINATE AXES

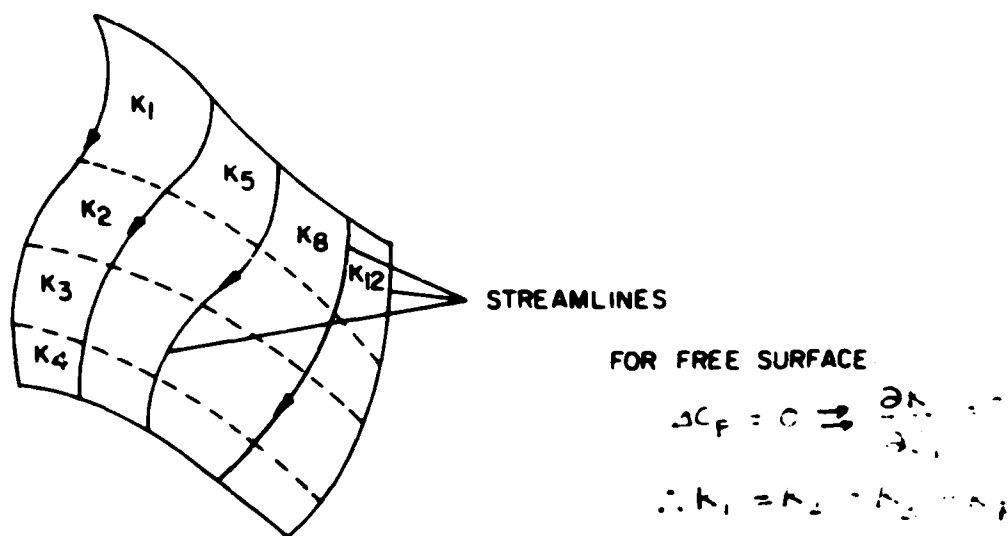


Fig. 9 GENERATION OF WAKE STRIPS

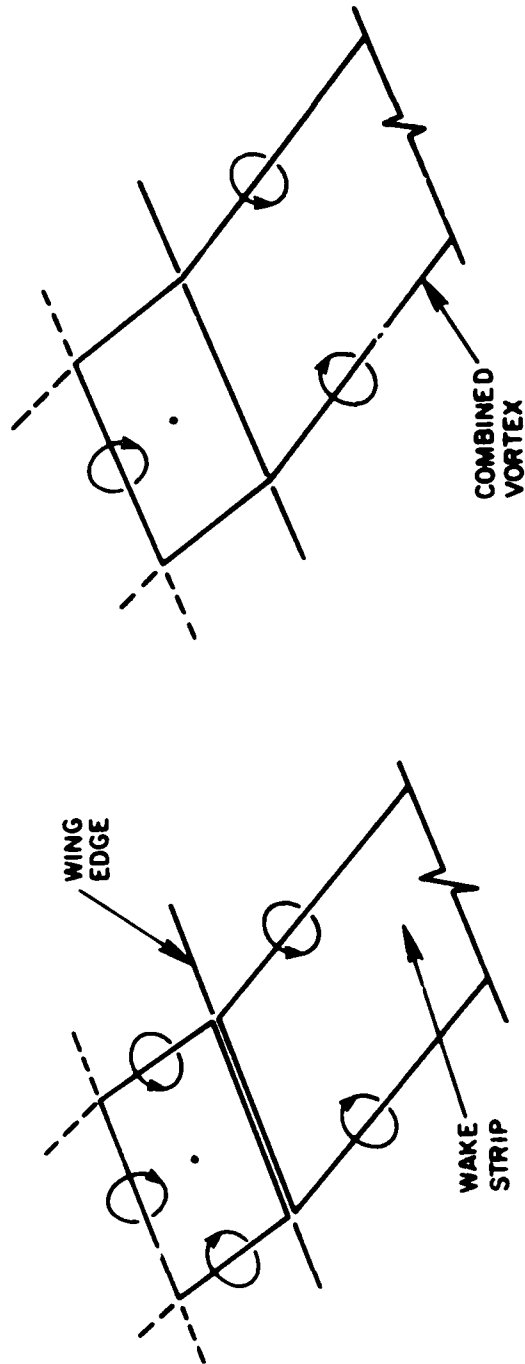


Fig. 10 ADDITION OF WAKE INFLUENCE TO EDGE BOX

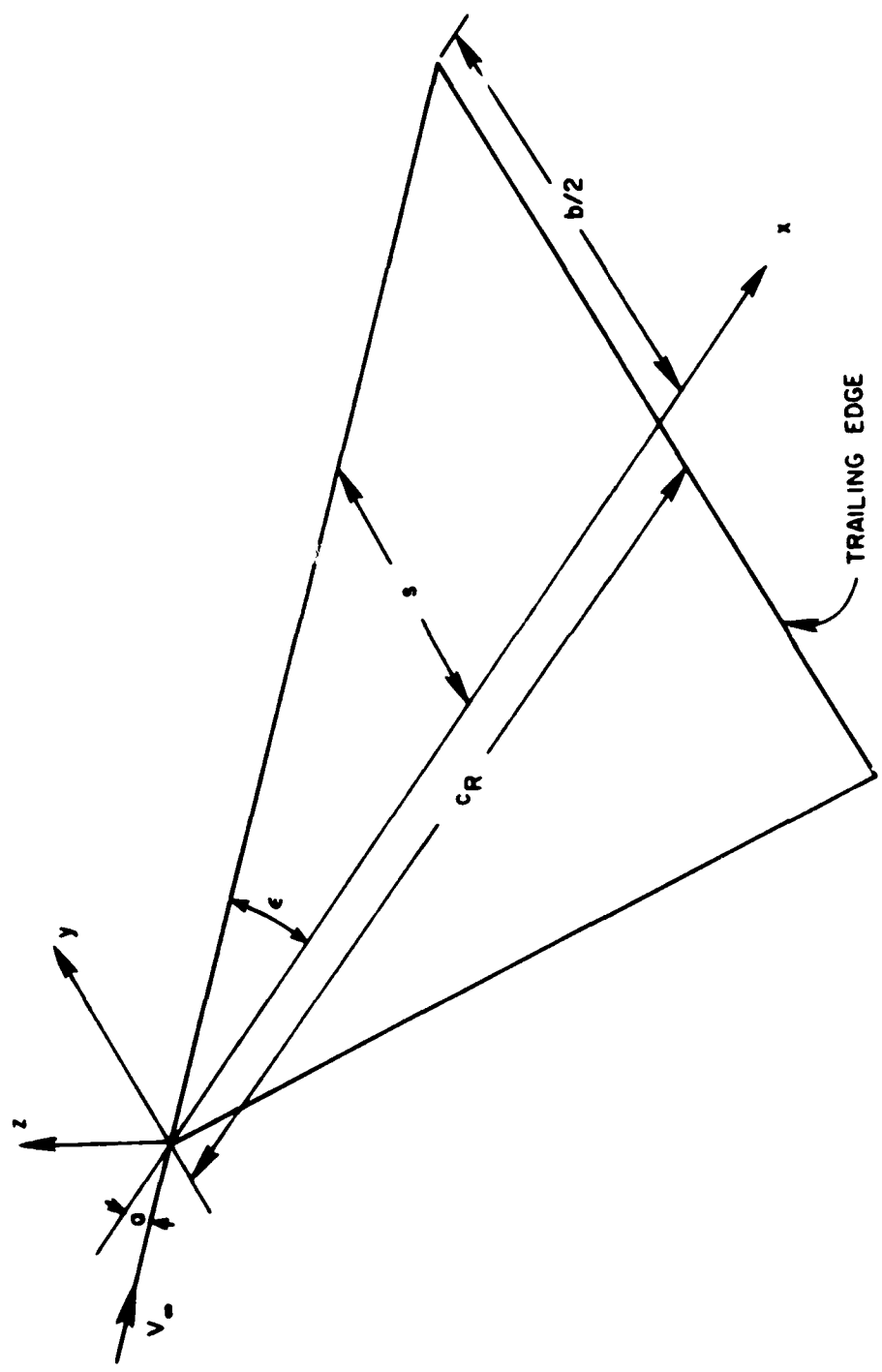


Fig. 11 SIGN CONVENTION

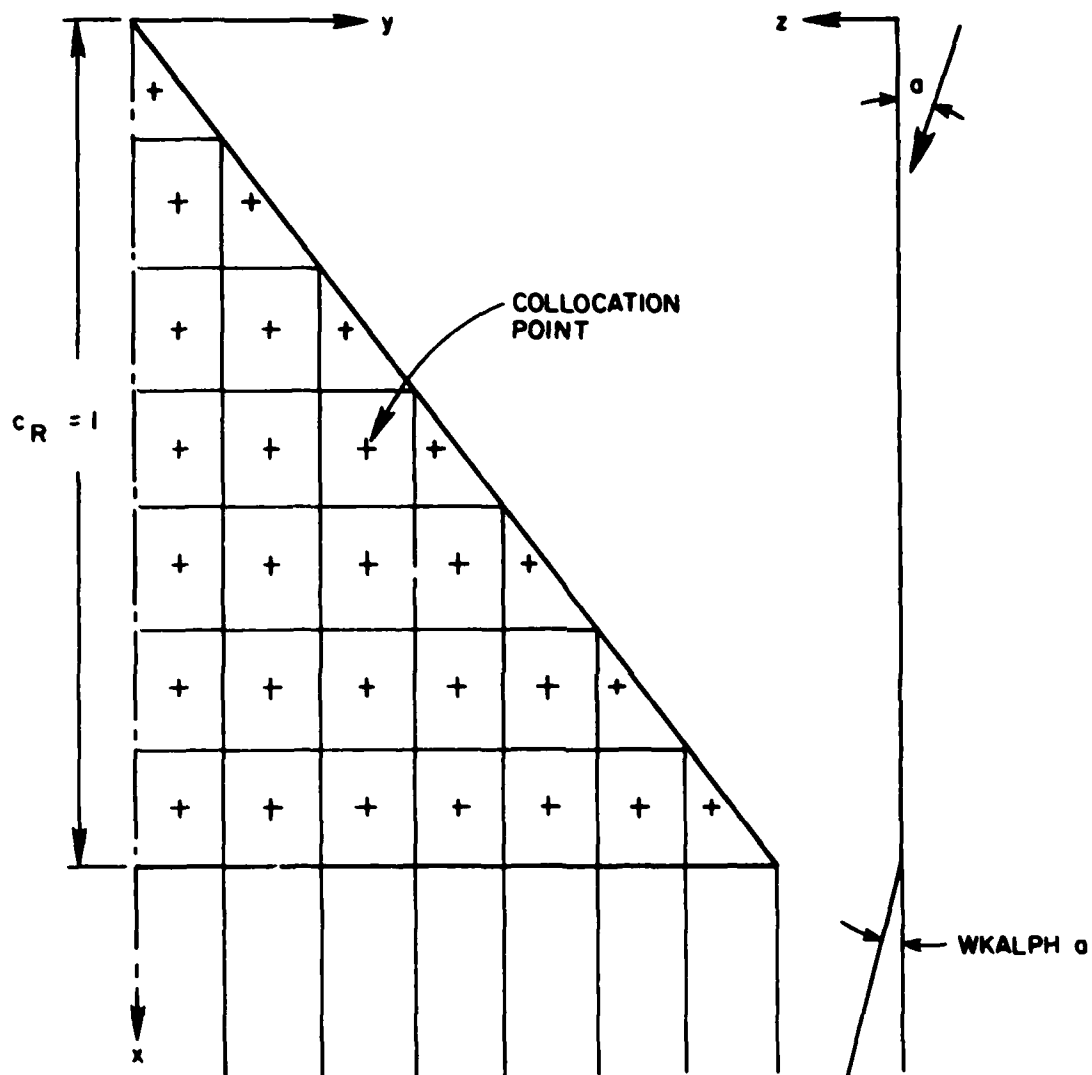


Fig. 12 ATTACHED FLOW MODEL

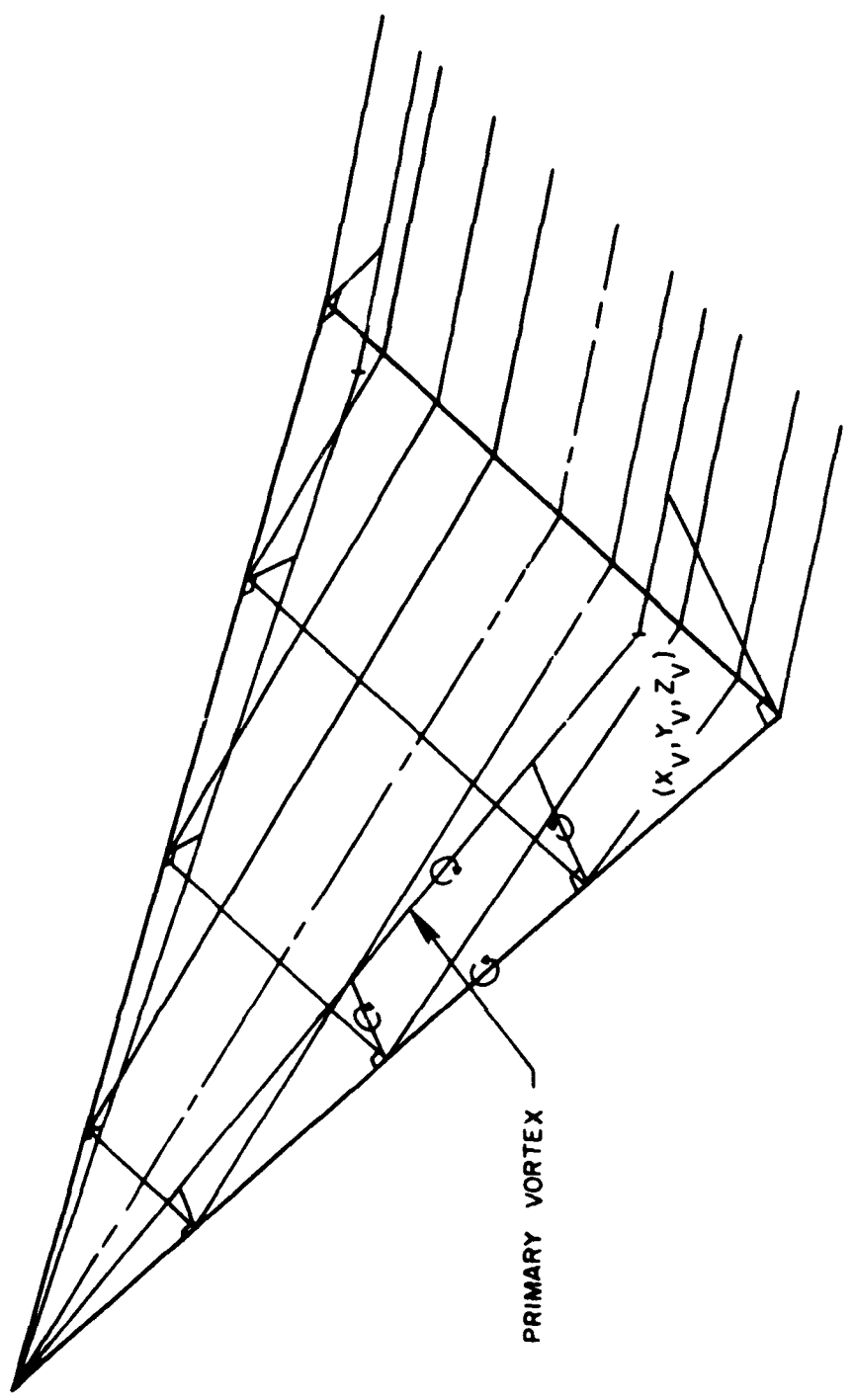


Fig. 13 DUPLICATION OF BROWN AND MICHAEL

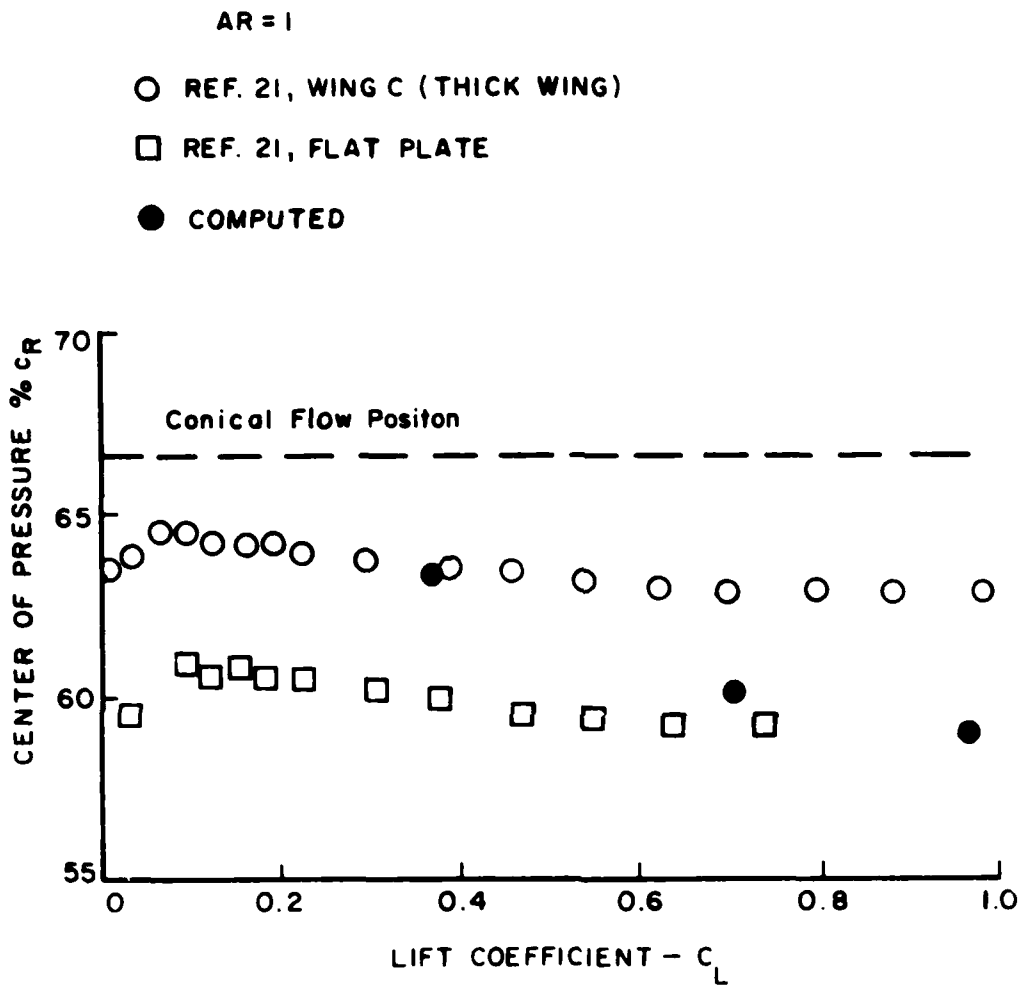


Fig. 15 CENTER OF PRESSURE PREDICTED BY THE FIXED - WAKE MODEL

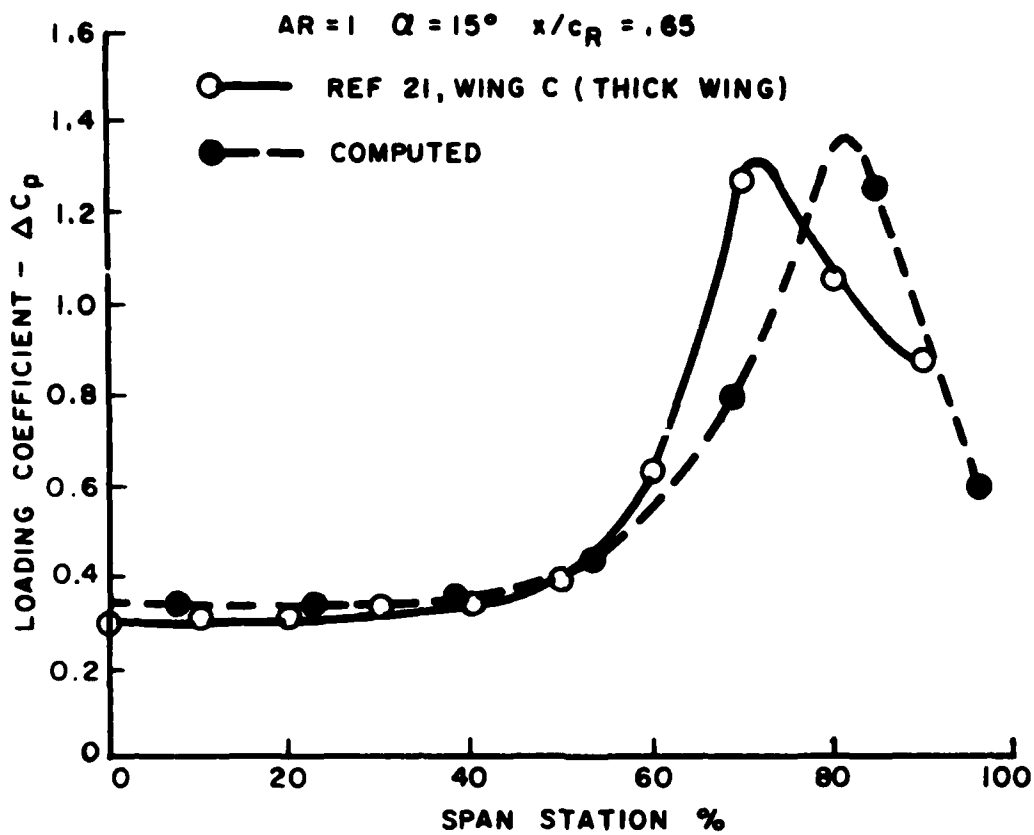


Fig. 16 COMPARISON OF PRESSURE DISTRIBUTION PREDICTED FOR THE FIXED - WAKE MODEL AND EXPERIMENTAL RESULTS

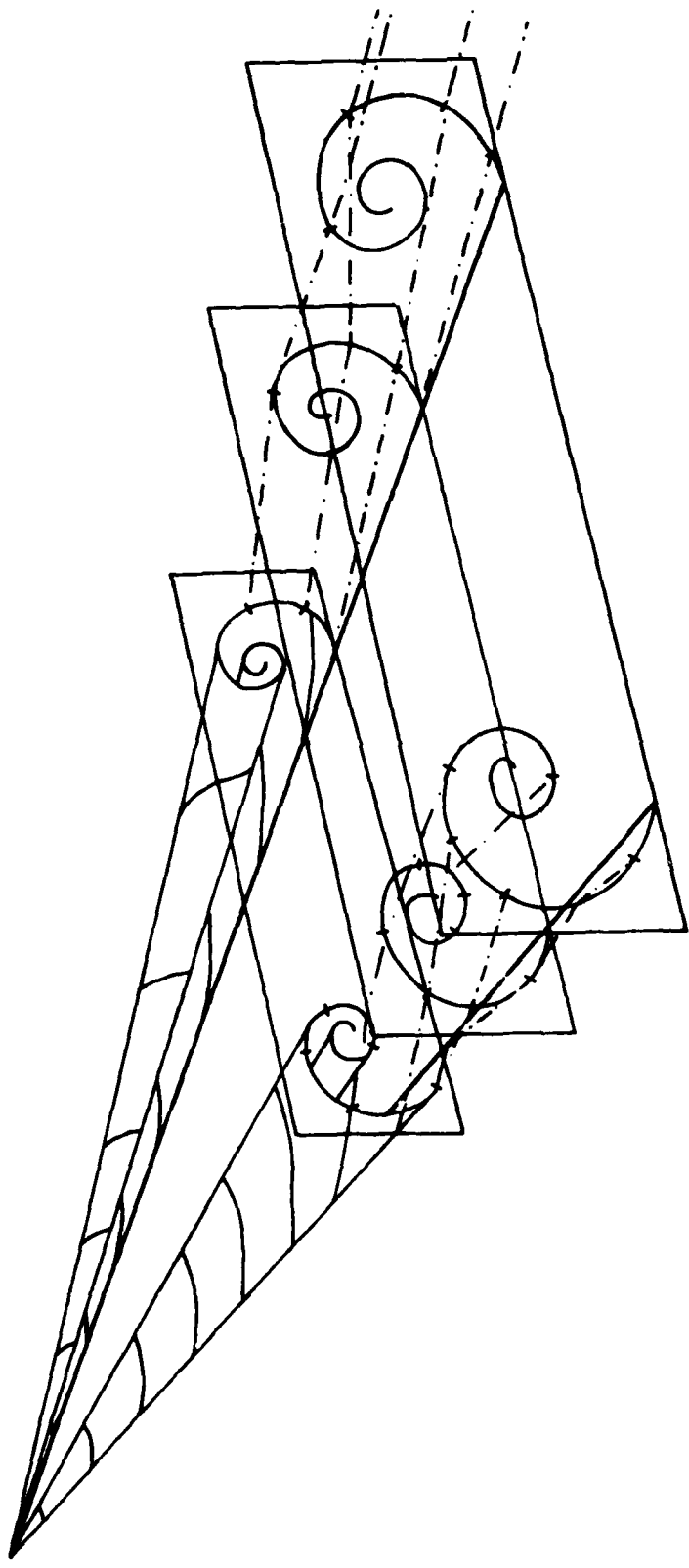


Fig. 17 FREE-WAKE MODEL OF LEADING-EDGE SHEET

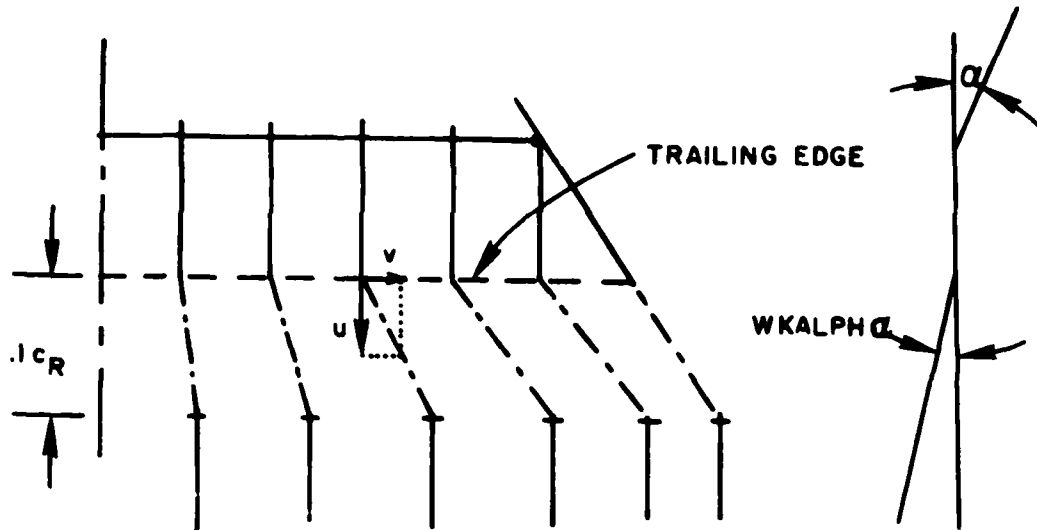


FIG. 18 TRAILING EDGE OF FREE-WAKE MODEL

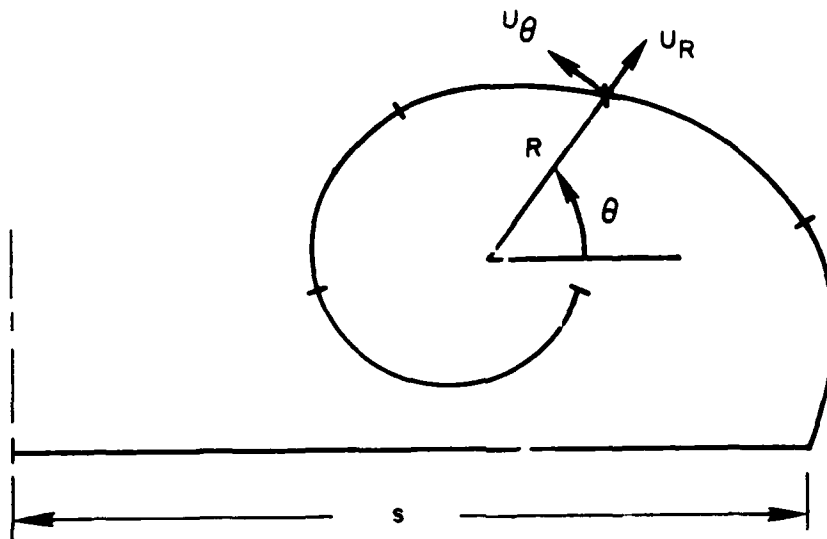


Fig. 19 POLAR COORDINATE SYSTEM

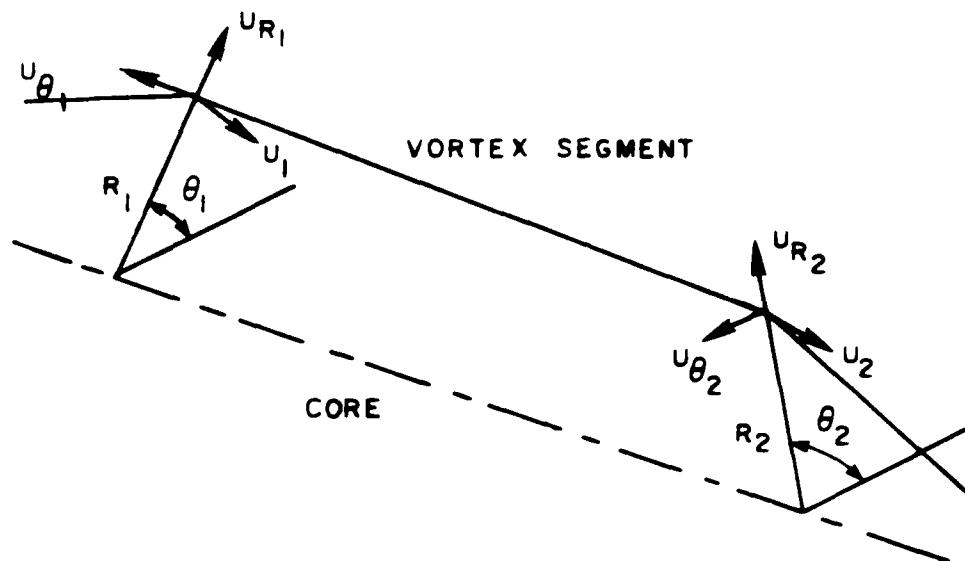


FIG. 20. FREE WAKE GEOMETRY PREDICTION.

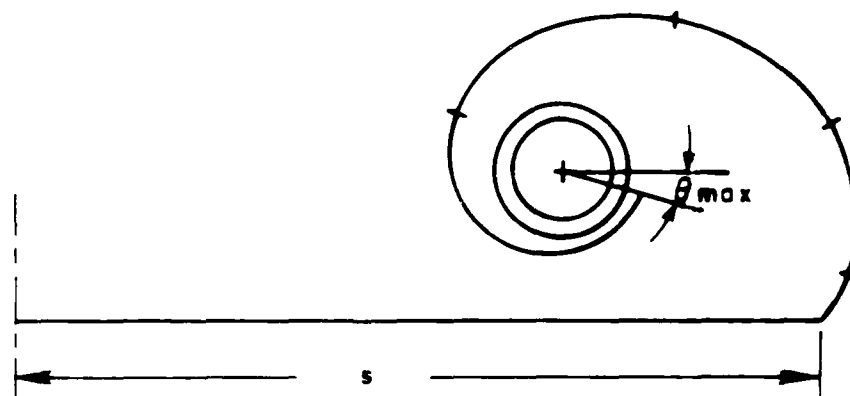


FIG. 21. FIXED SIZE CORE.

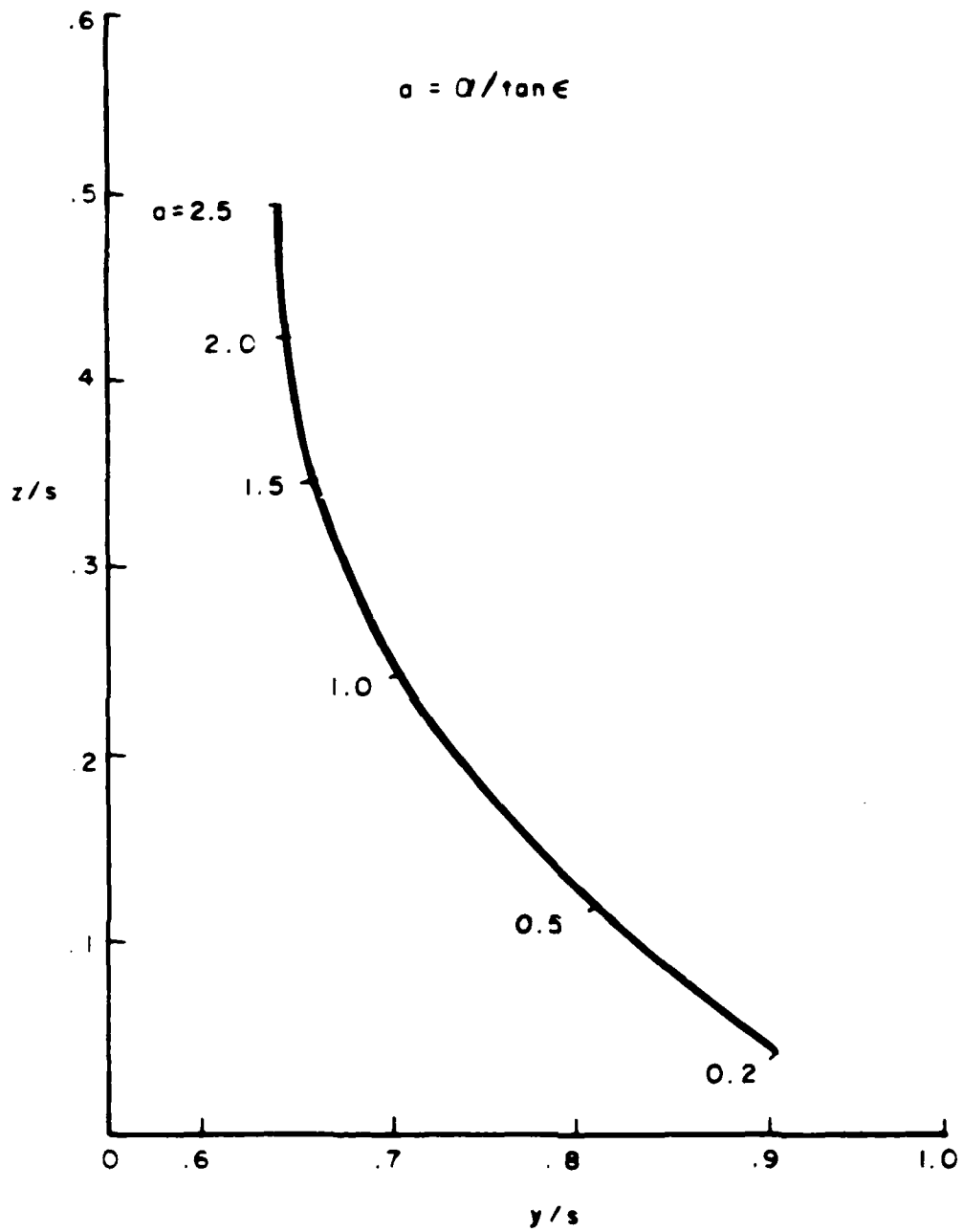


Fig. 22 VORTEX CORE POSITION OF SMITH



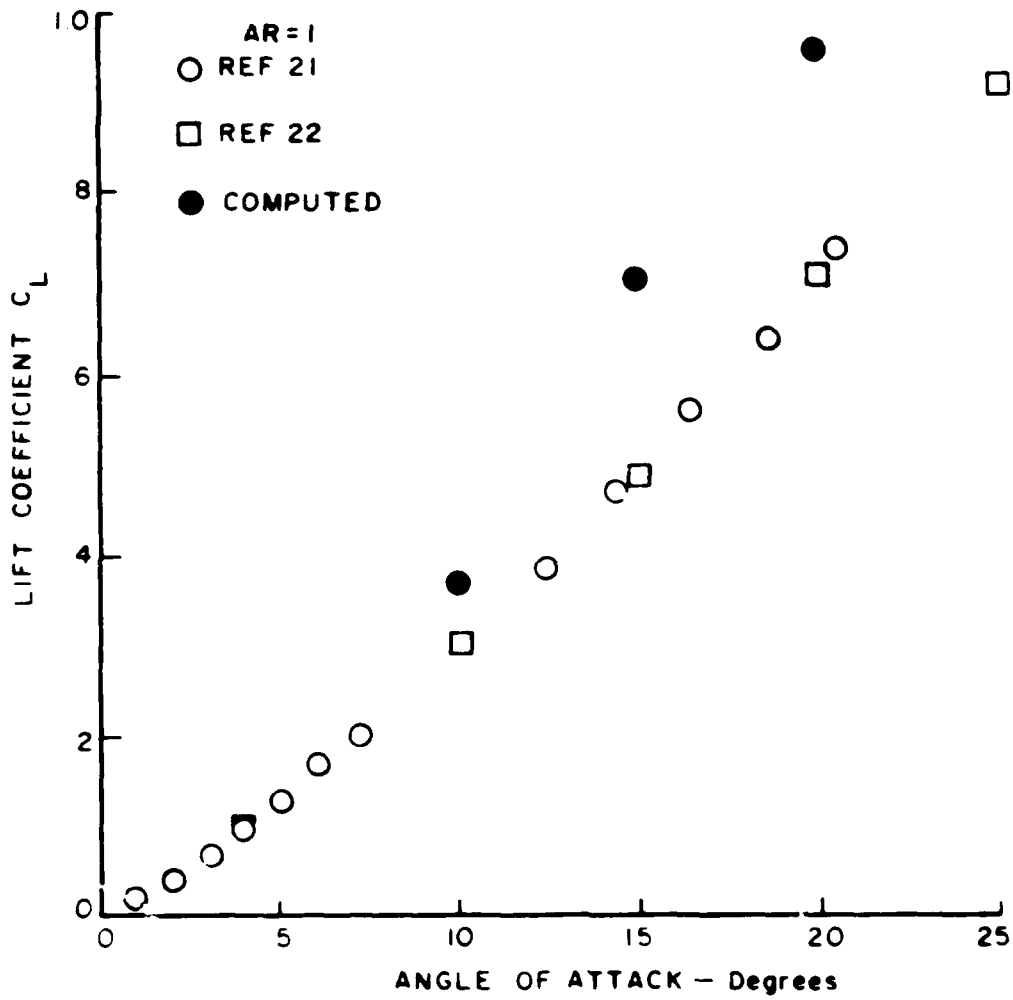


FIG. 24. LIFT CURVE OF REF. AXE MODEL.

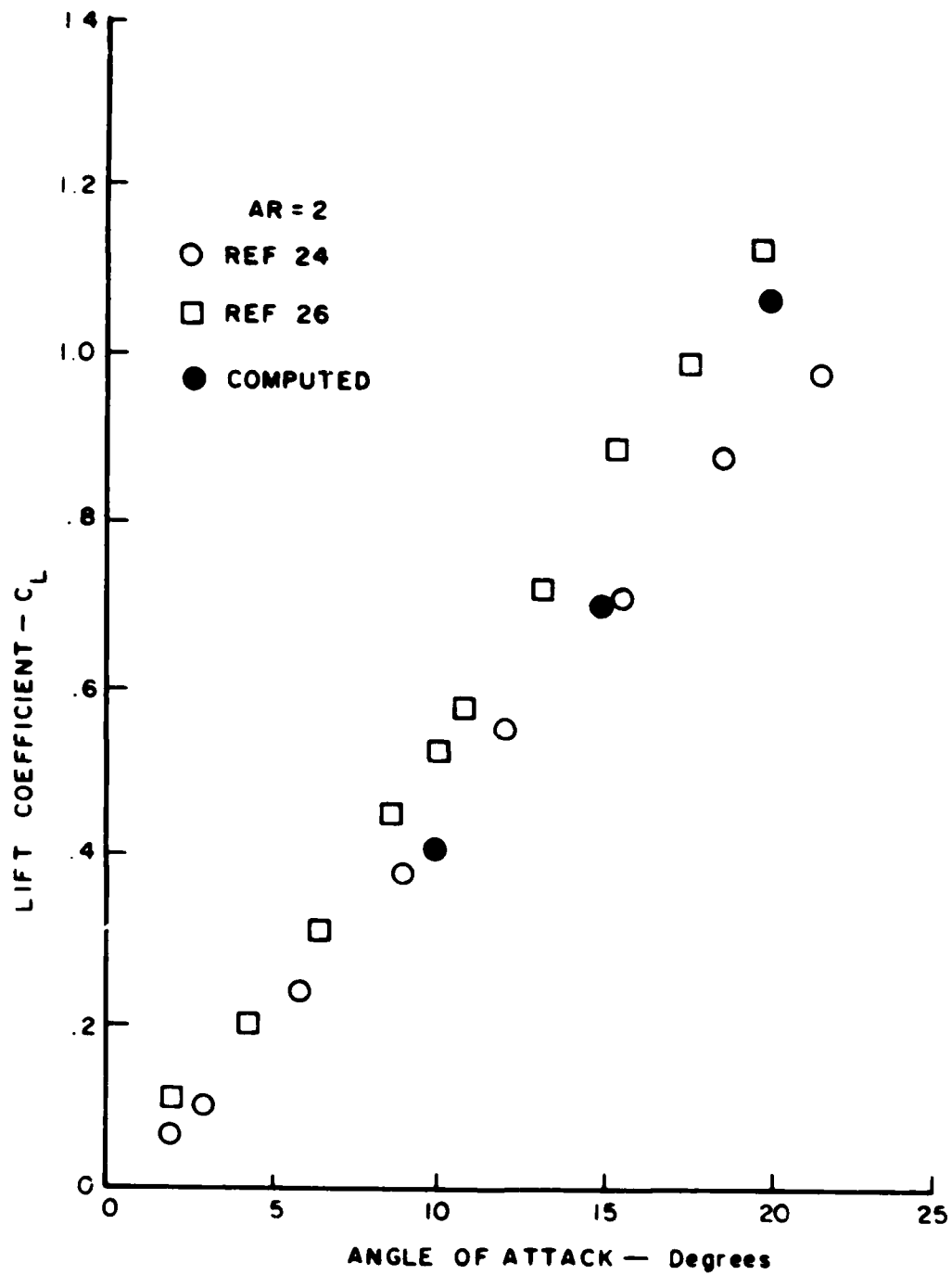


Fig. 25 LIFT CURVE OF SPLE WAKE MODEL

- AR = 1
- REF 21, WING C (THICK WING)
  - REF 21, FLAT PLATE
  - COMPUTED

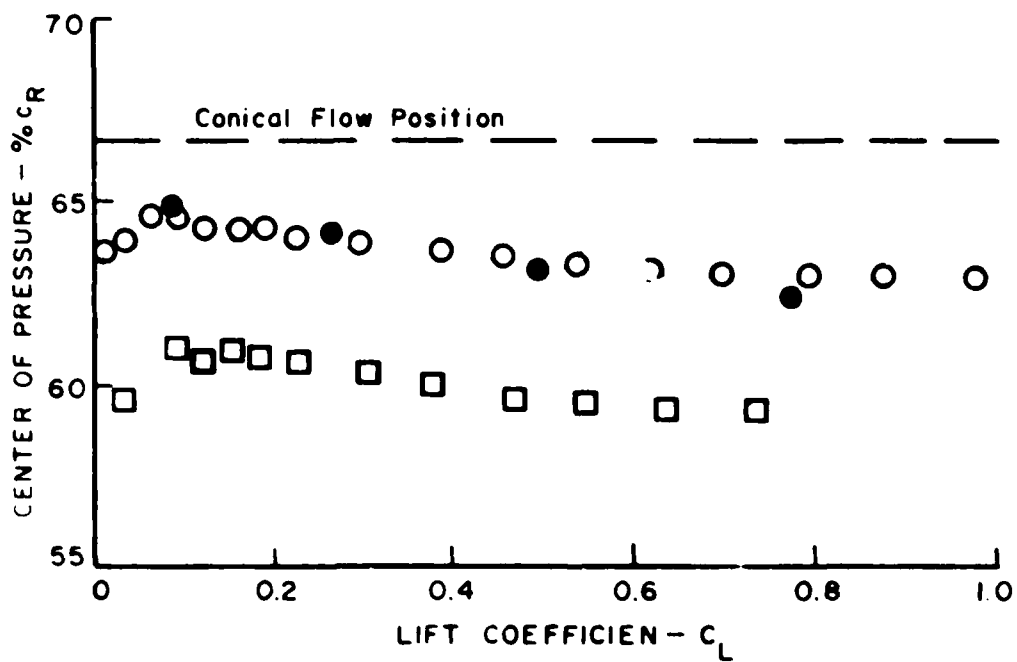


Fig. 26 CENTER OF PRESSURE PREDICTED BY FREE FLOW MODEL

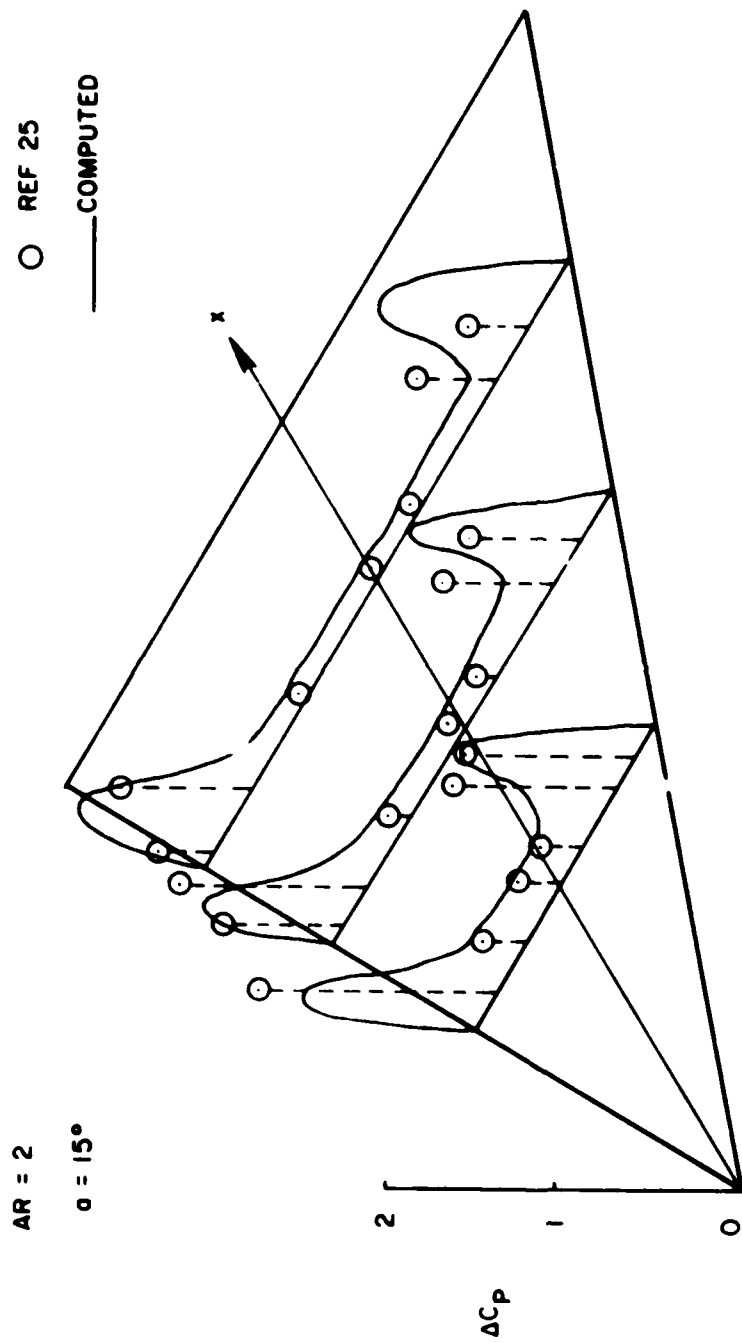


Fig. 27 FREE-WAKE MODEL LOADING DISTRIBUTION

Aspect Ratio 2  $\alpha = 20^\circ$

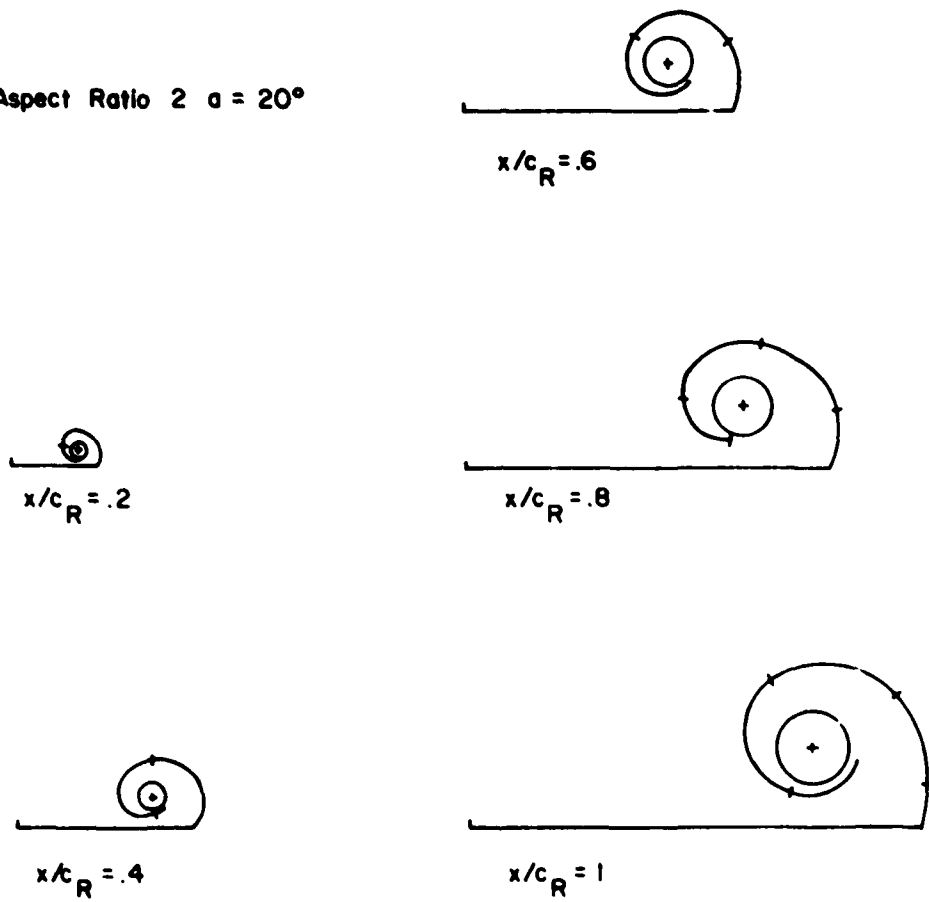


Fig. 28. CONDENSED LEADING EDGE SHEET GROWTH

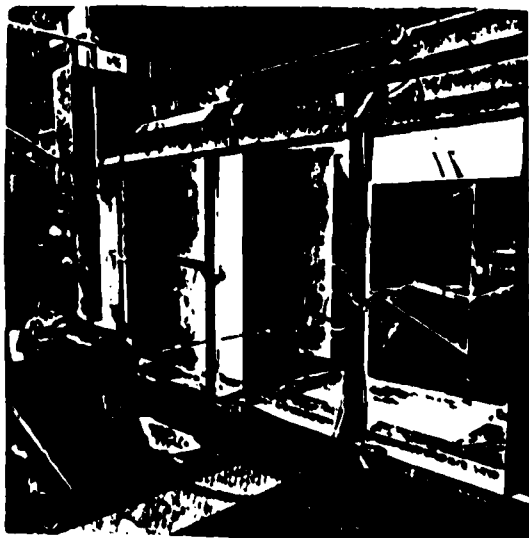
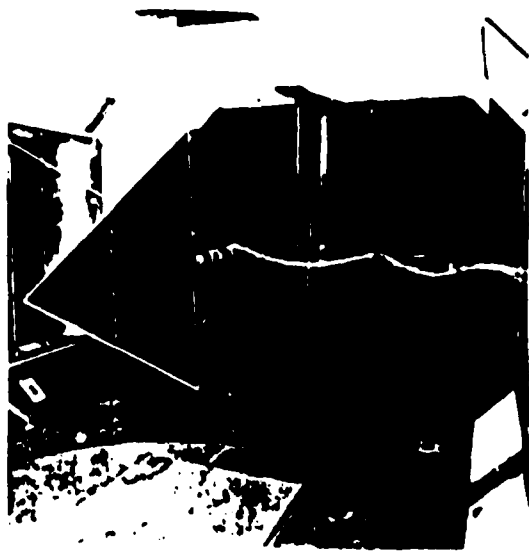


Fig. 29 DETAILS OF TEST EQUIPMENT

Reproduced from  
best available copy. 

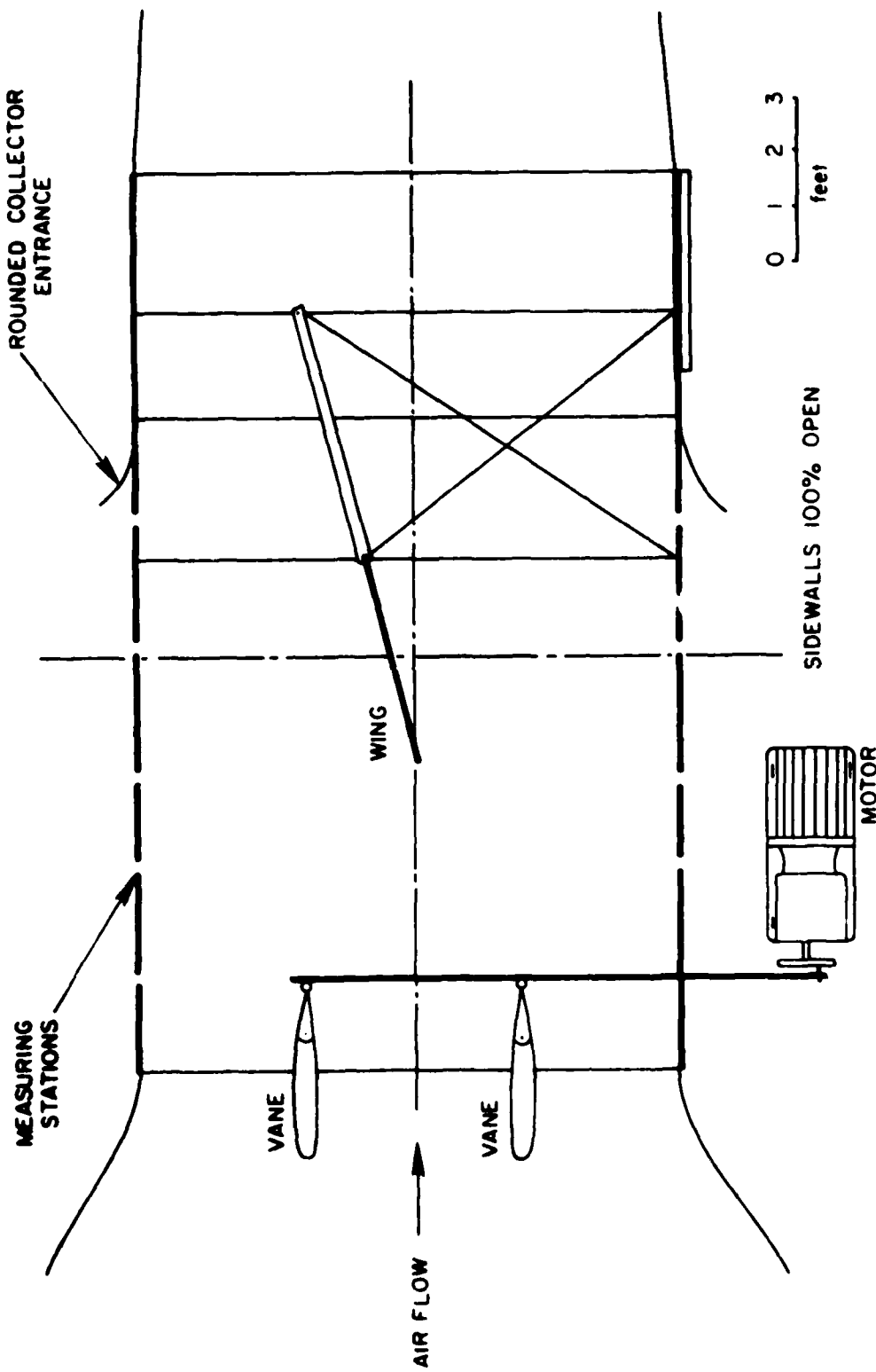
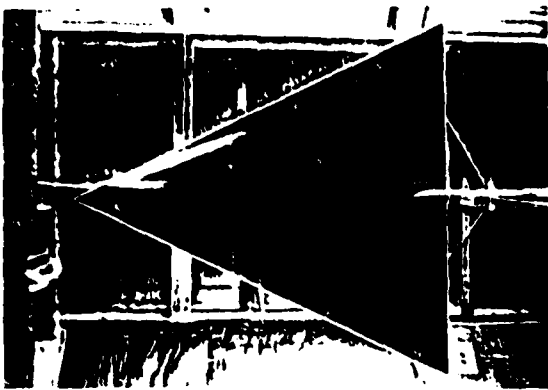
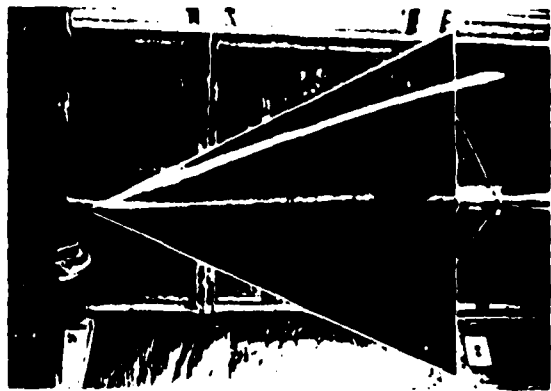


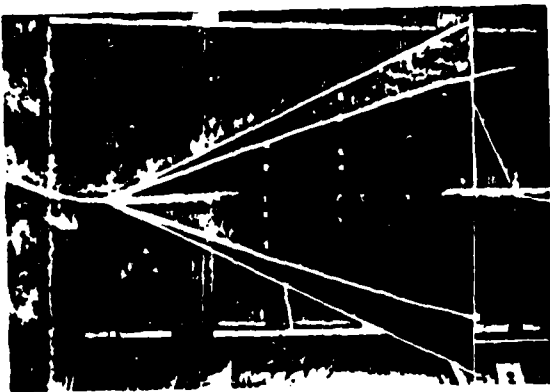
Fig. 30 GUST GENERATOR AND AIRFOIL



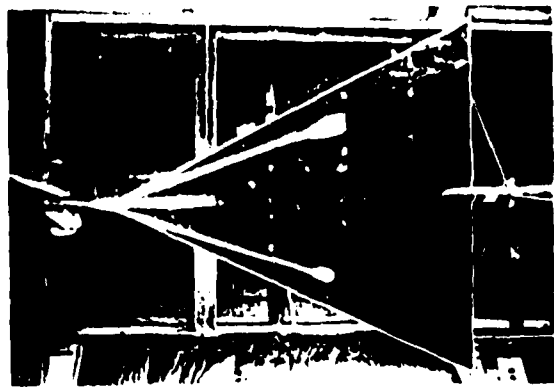
$\alpha = 5^\circ$



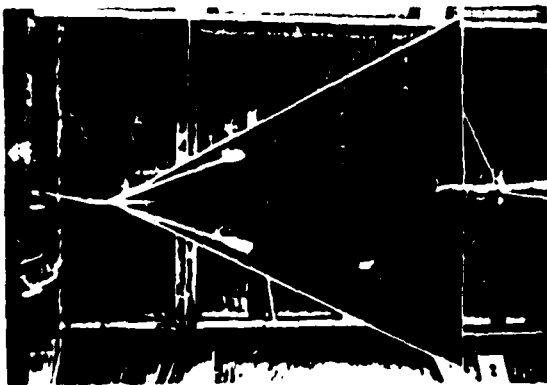
$\alpha = 10^\circ$



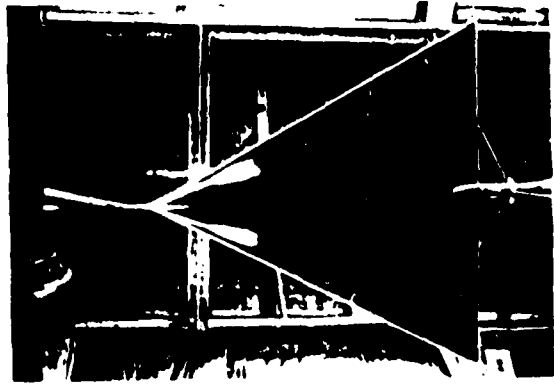
$\alpha = 15^\circ$



$20^\circ$

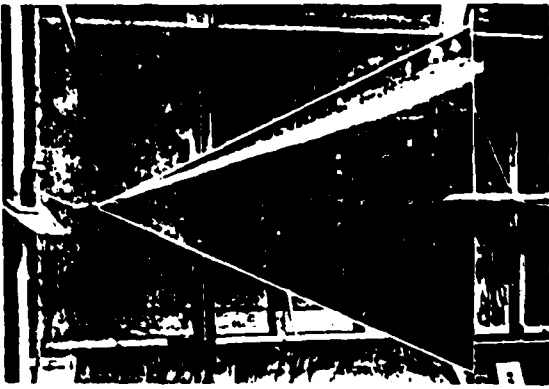


$25^\circ$

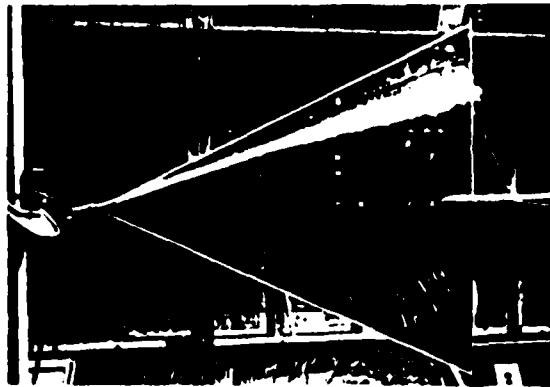


$30^\circ$

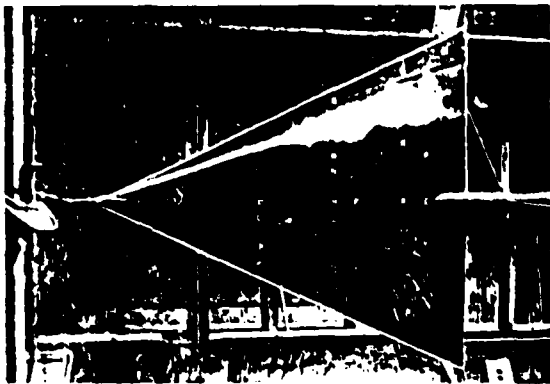
Fig. 31 VORTEX FLOW VISUALIZATION - STEADY FLOW



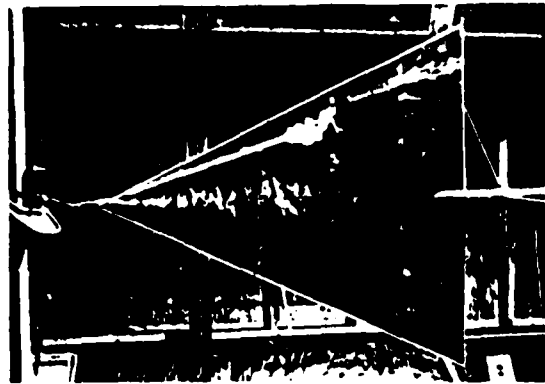
$\alpha = 17.3^\circ$



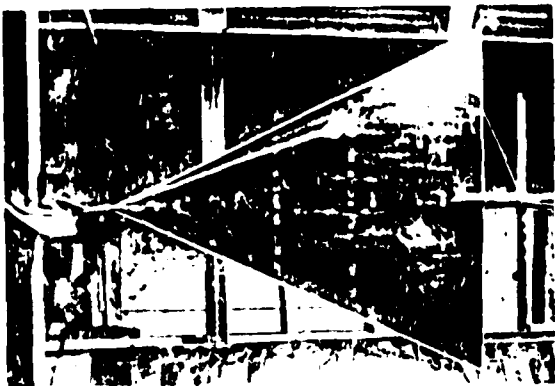
$\alpha = 22.1^\circ$



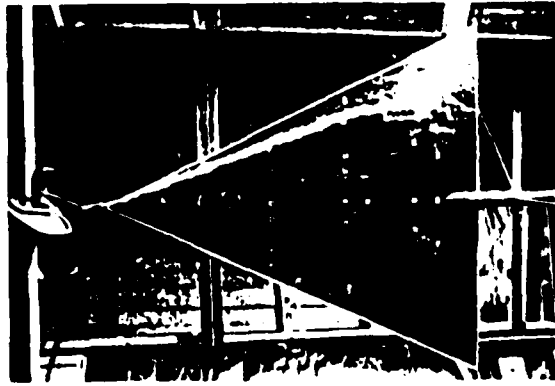
$\alpha = 22.7^\circ$  (decreasing)



$\alpha = 15.2^\circ$



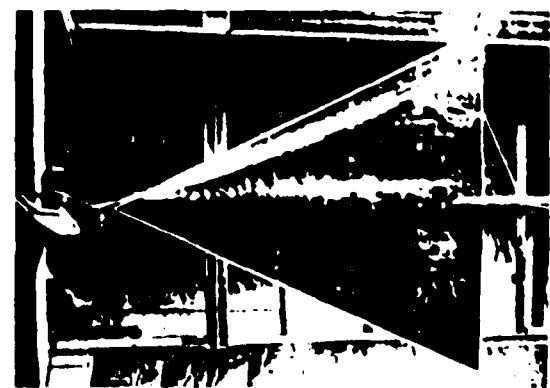
$\alpha = 10.1^\circ$



$\alpha = 5.1^\circ$

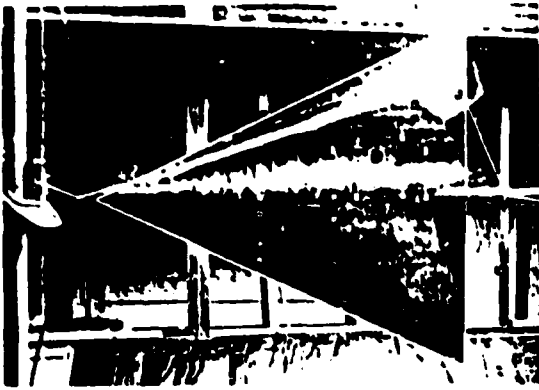


$\alpha = 0.1^\circ$

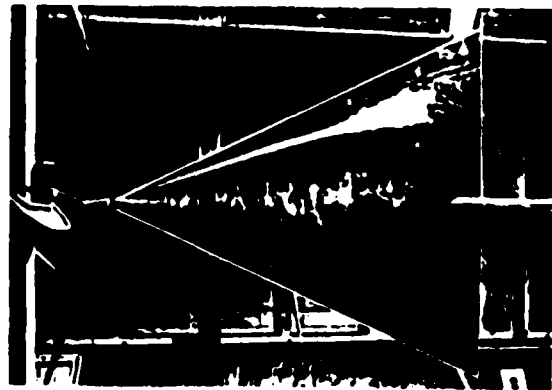


$\alpha = 0.1^\circ$

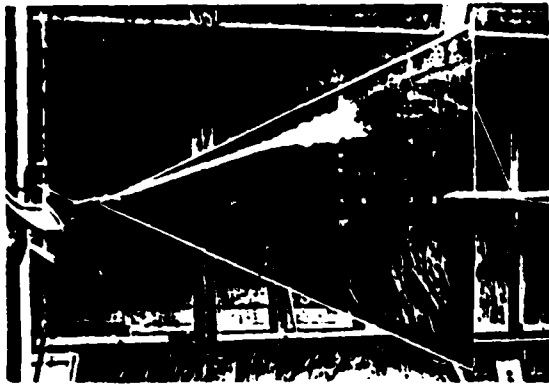
Fig. 32 VORTEX FLOW VISUALIZATION



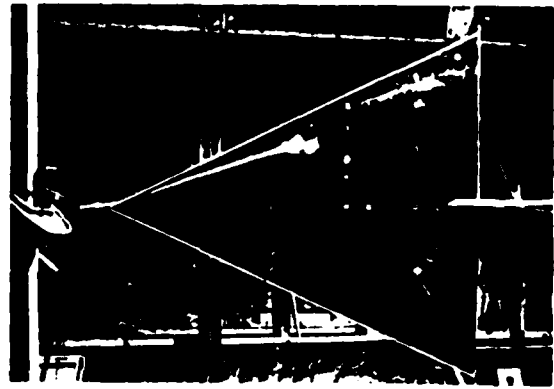
$\alpha = 15.3^\circ$



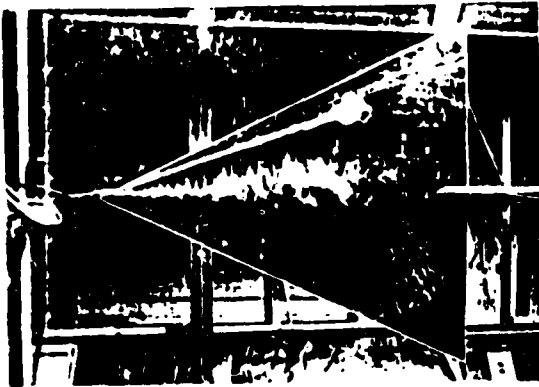
$\alpha = 20.9^\circ$



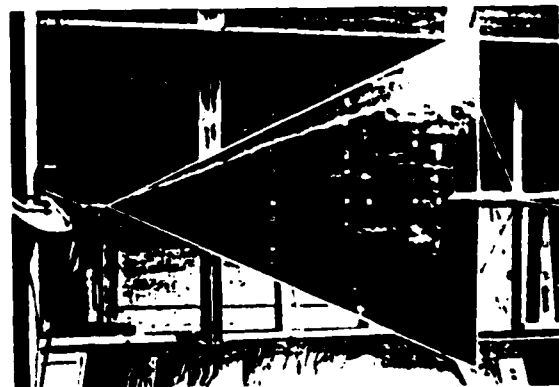
$\alpha = 23.0^\circ$



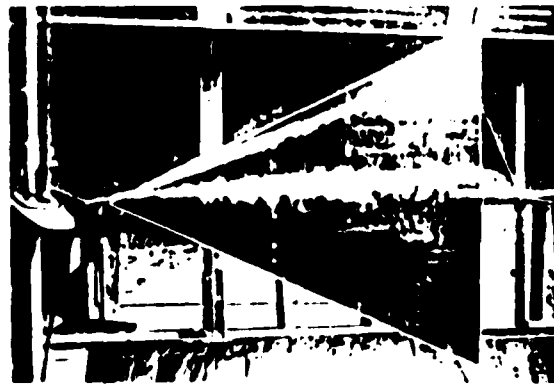
$\alpha = 20.5^\circ$



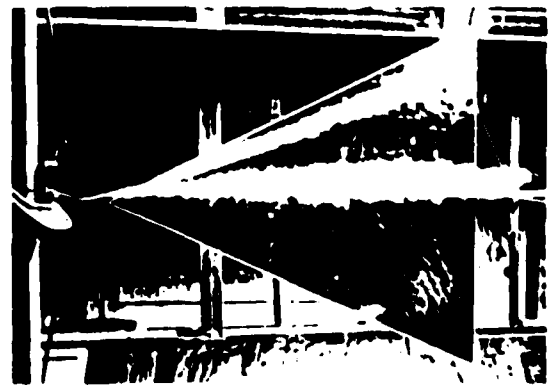
$\alpha = 14.7^\circ$



$\alpha = 9.1^\circ$



$\alpha = 2.0^\circ$



$\alpha = 1.5^\circ$

Fig. 33 VORTEX FLOW VISUALIZATION - 1

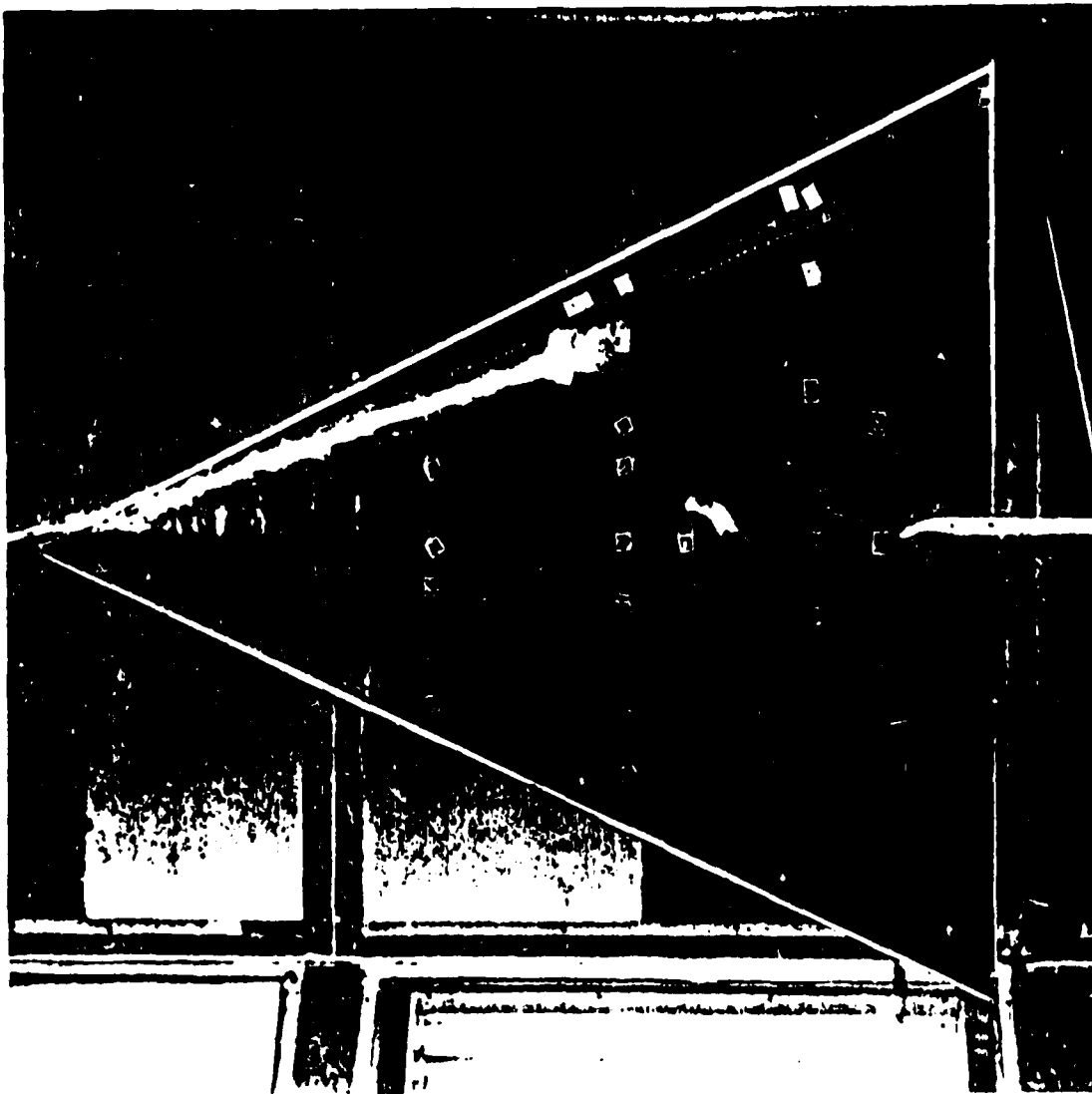


Fig. 34 DETAILS OF A HELICAL TYPE BURST

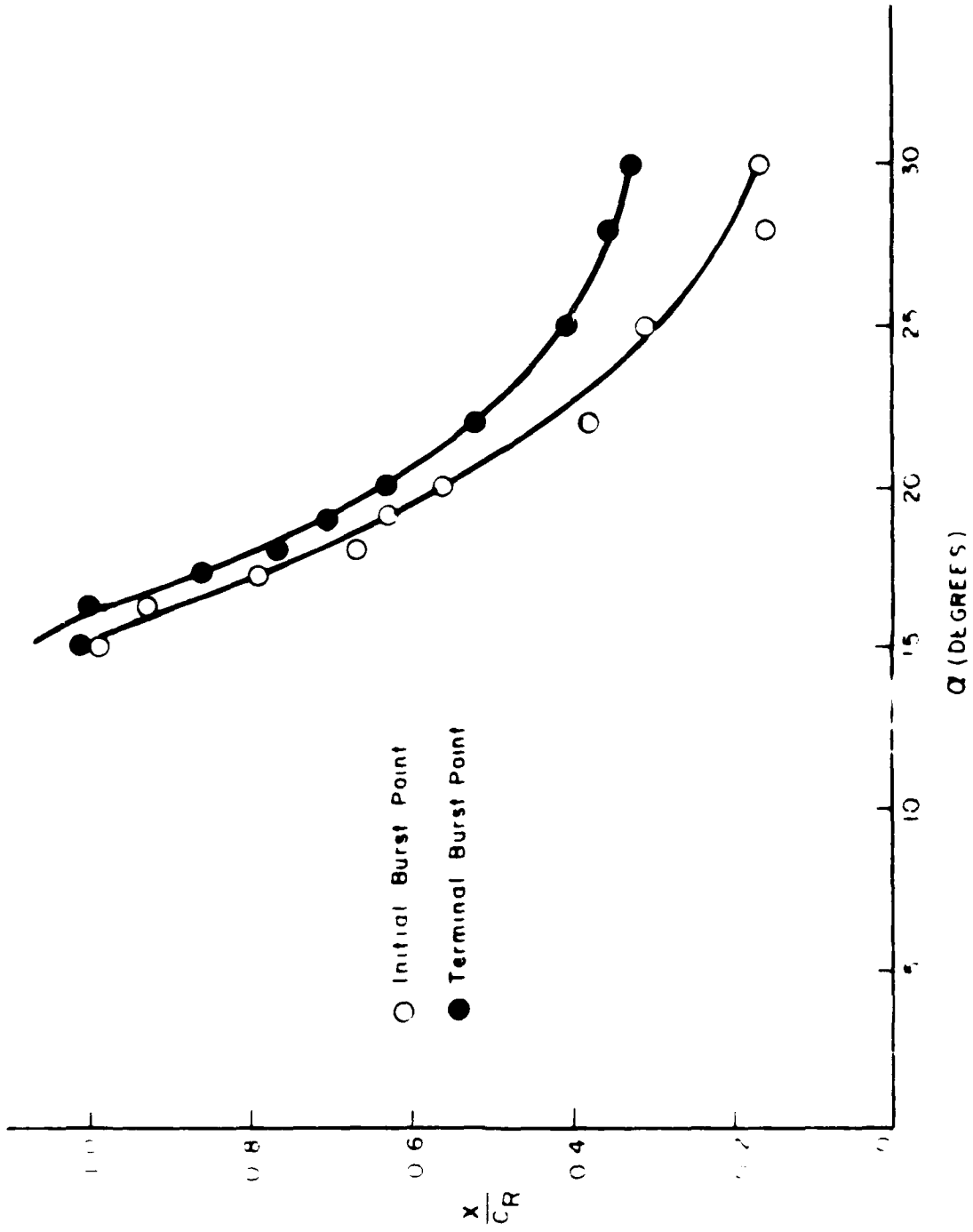


Fig. 35. VORTEX BURST - STEADY FLOW

$AB = 2$   
 $CD = 4''$   
 $s = 2''$

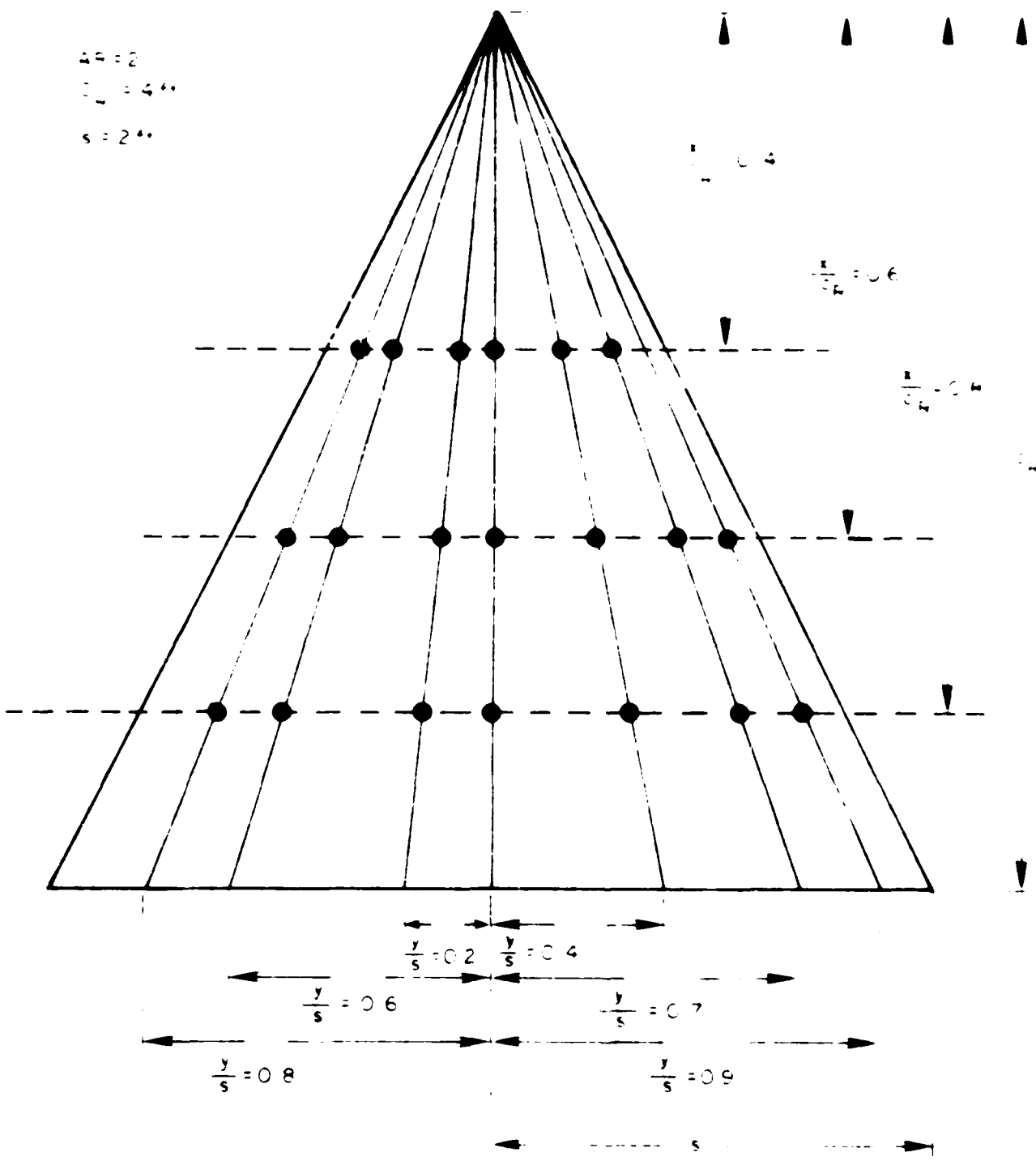


FIG. 26 POSITION OF POINTS ON SURFACE

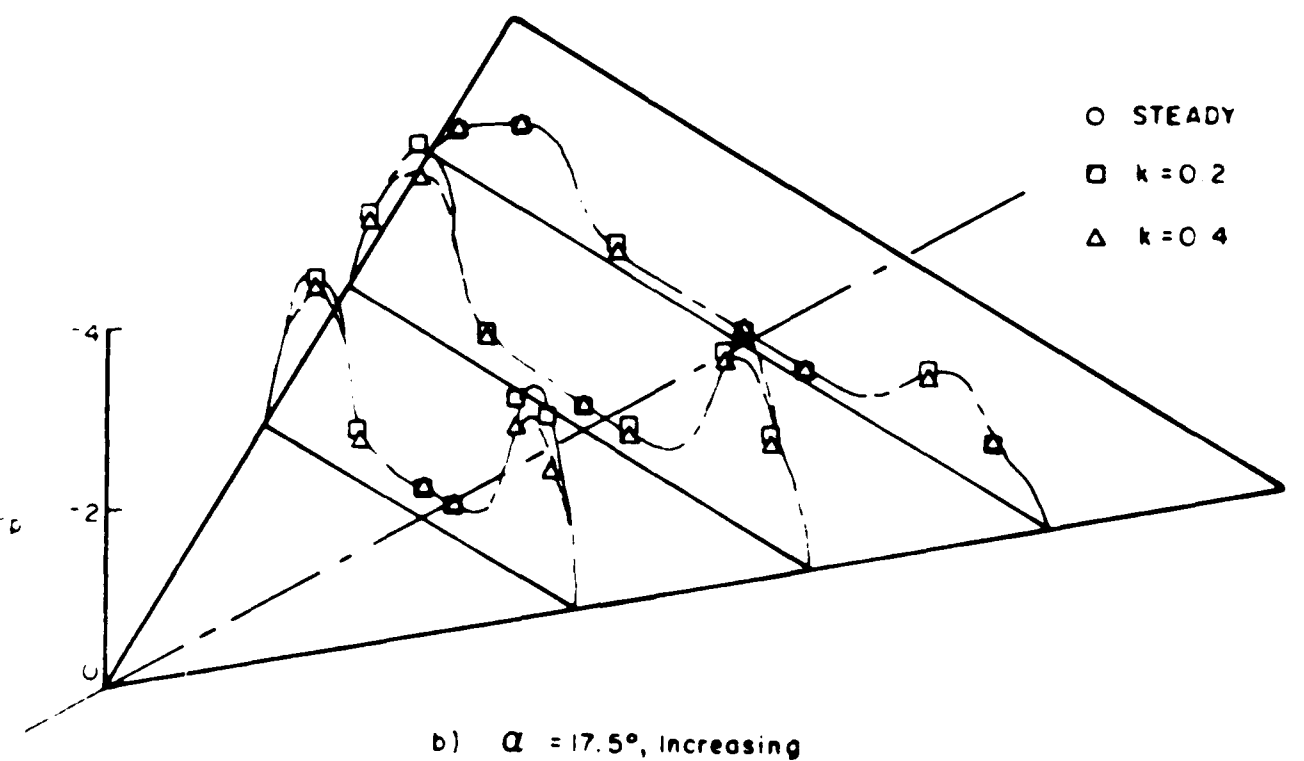
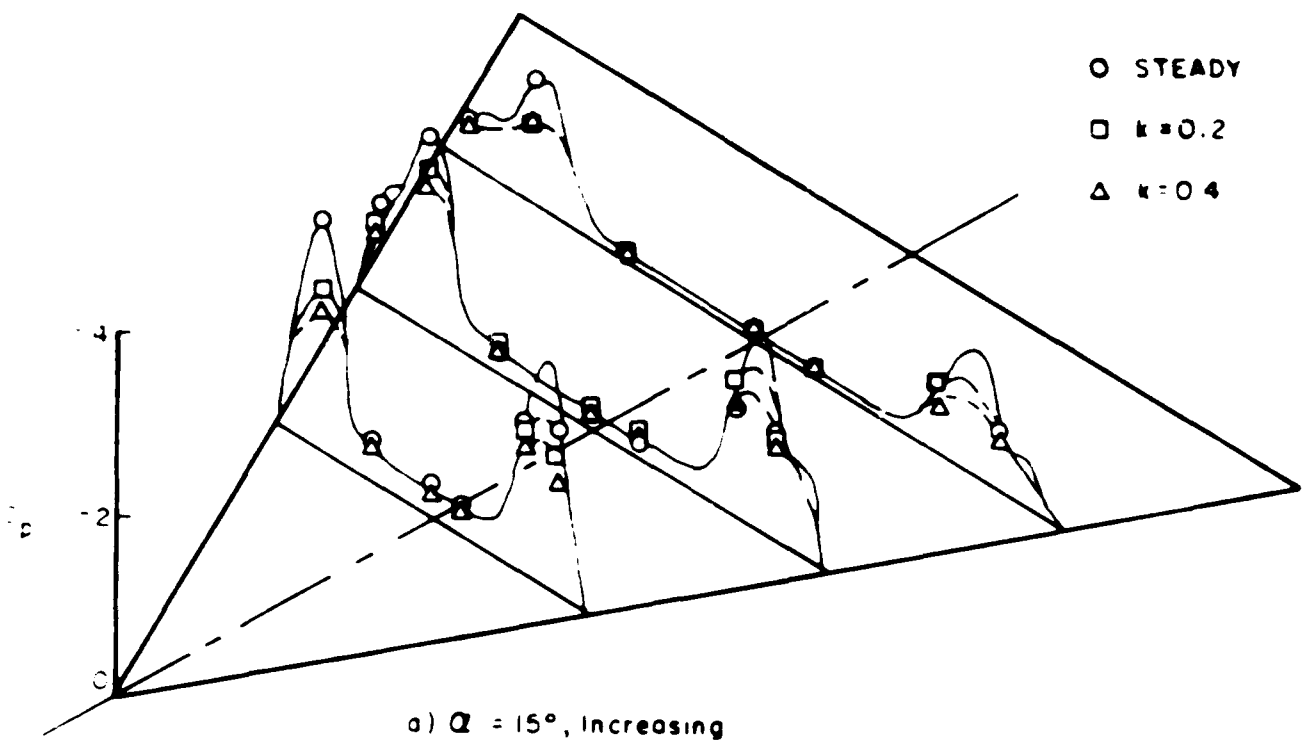
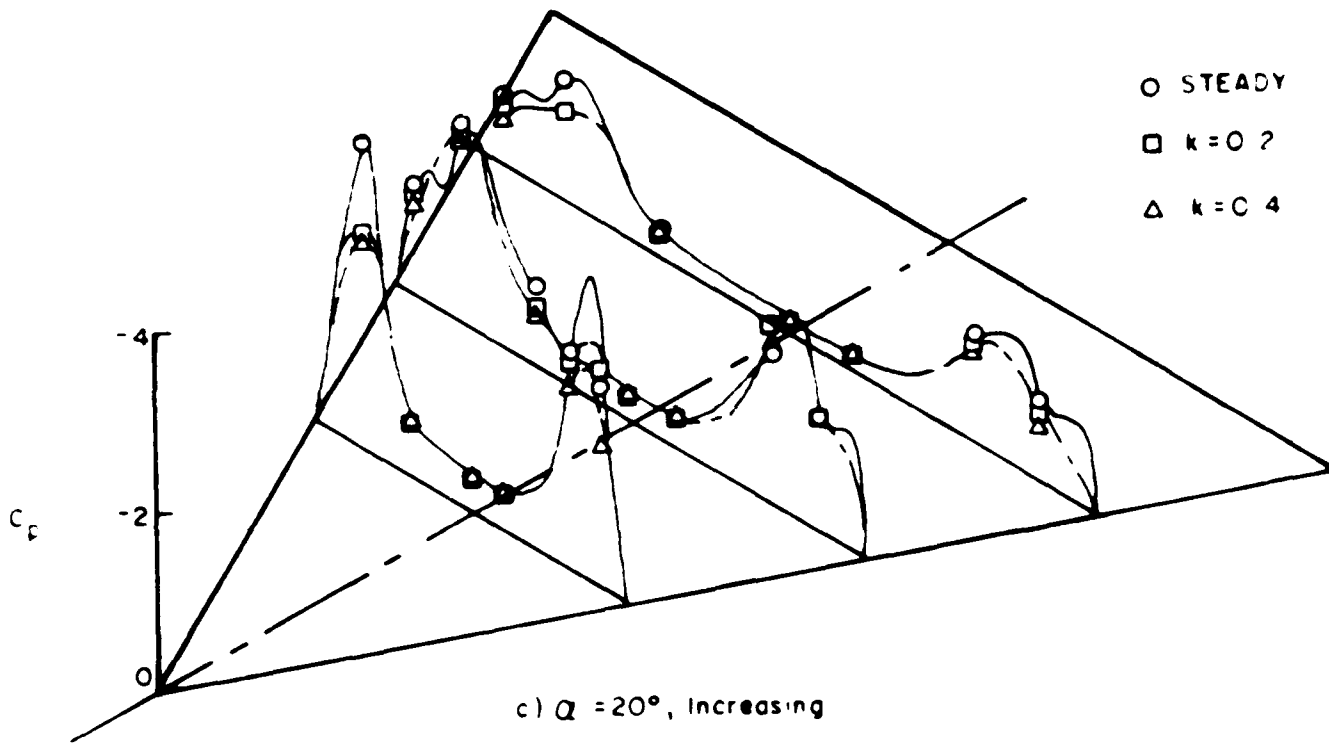
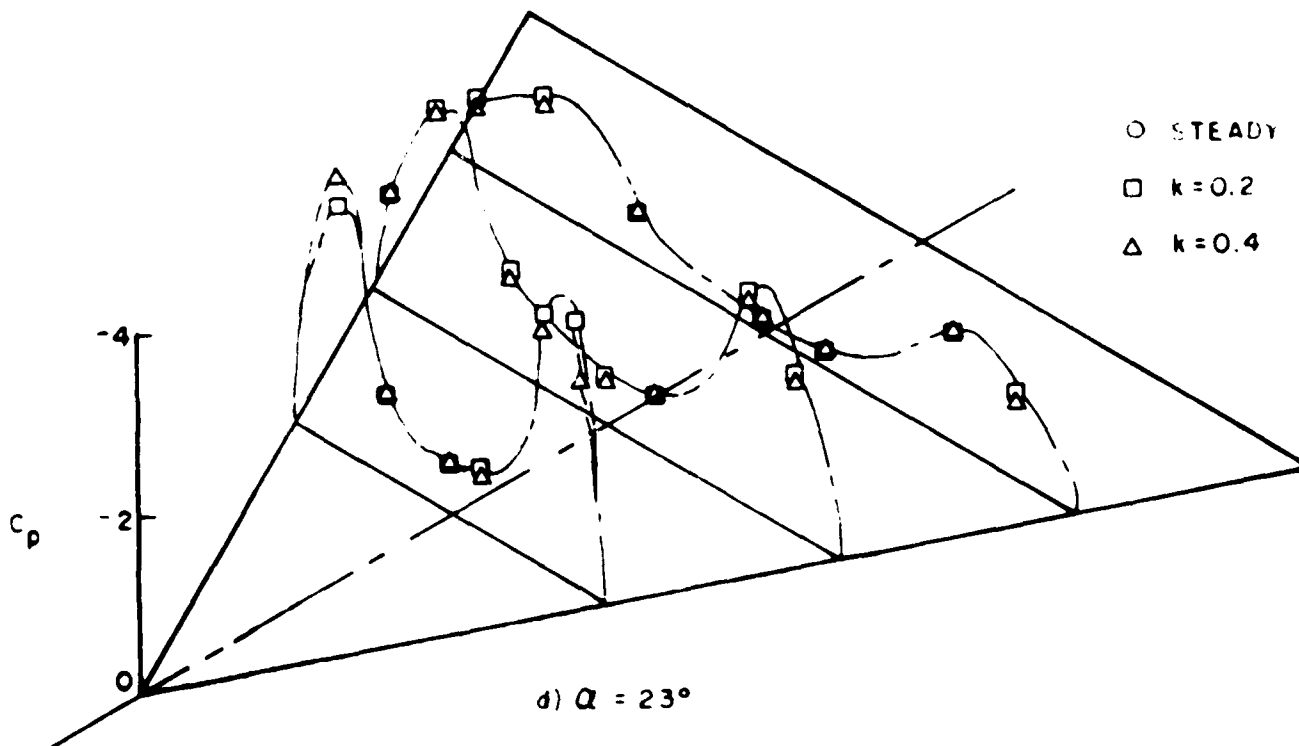


FIG. 17. PRESSURE DISTRIBUTIONS ON A DELTA WING

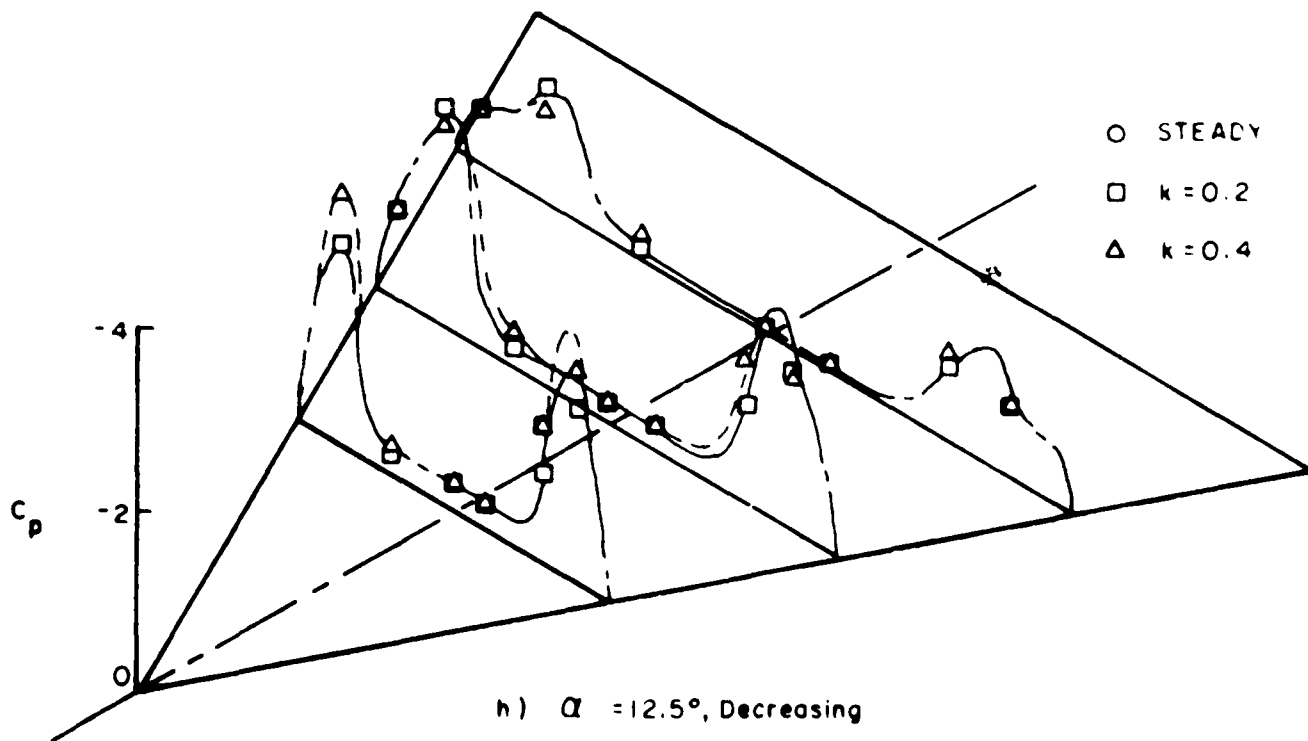
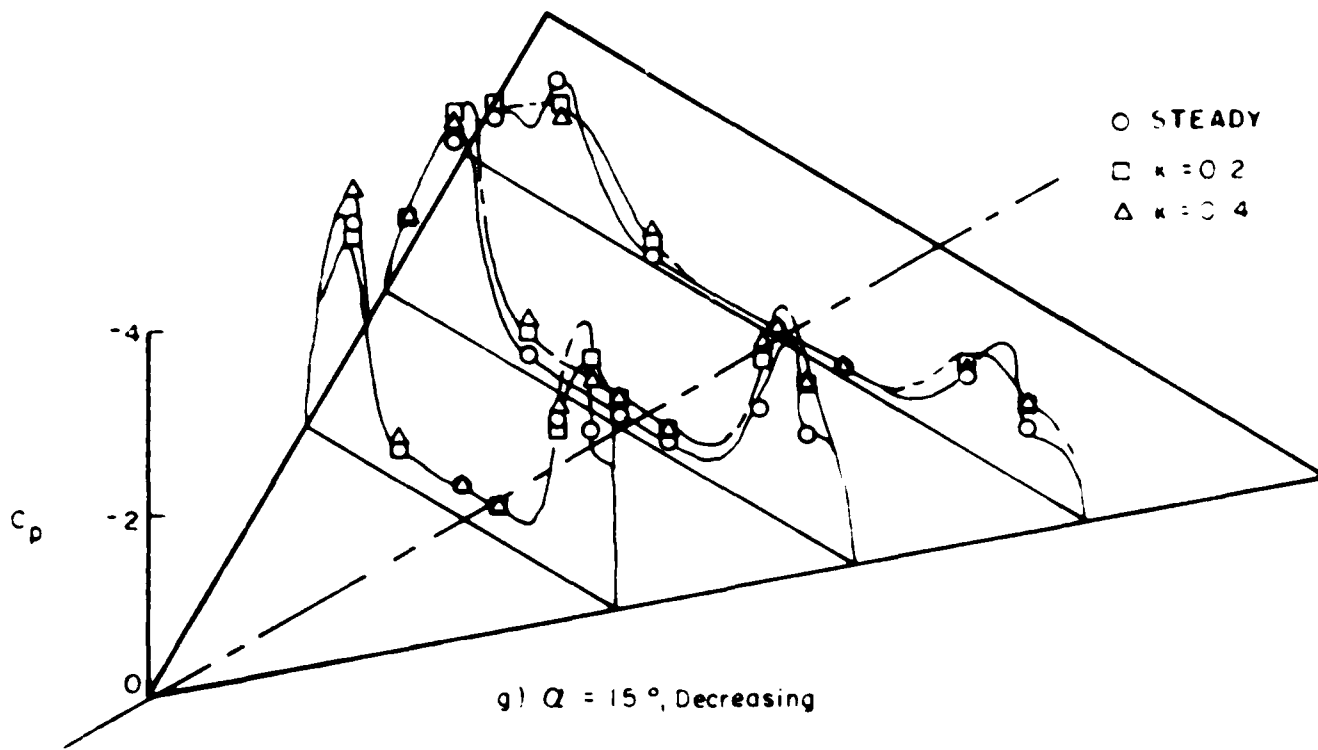


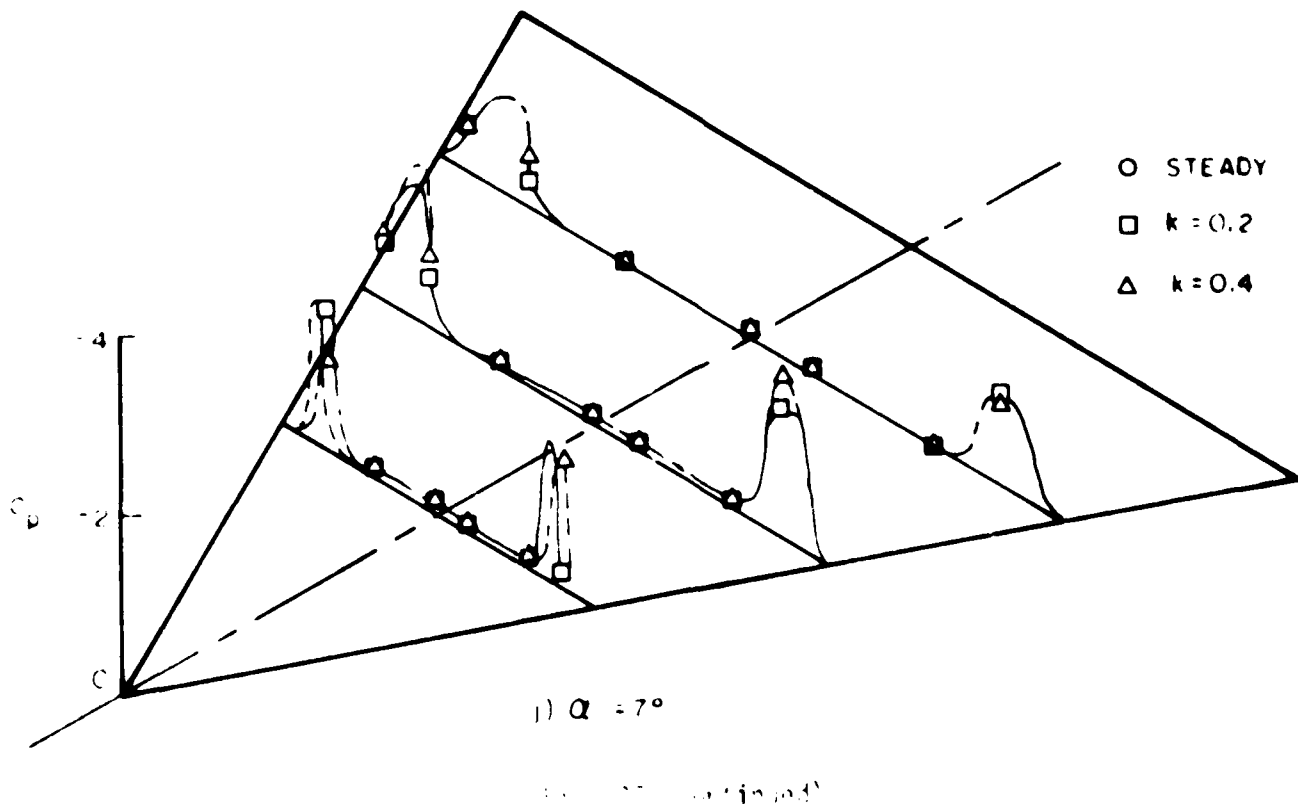
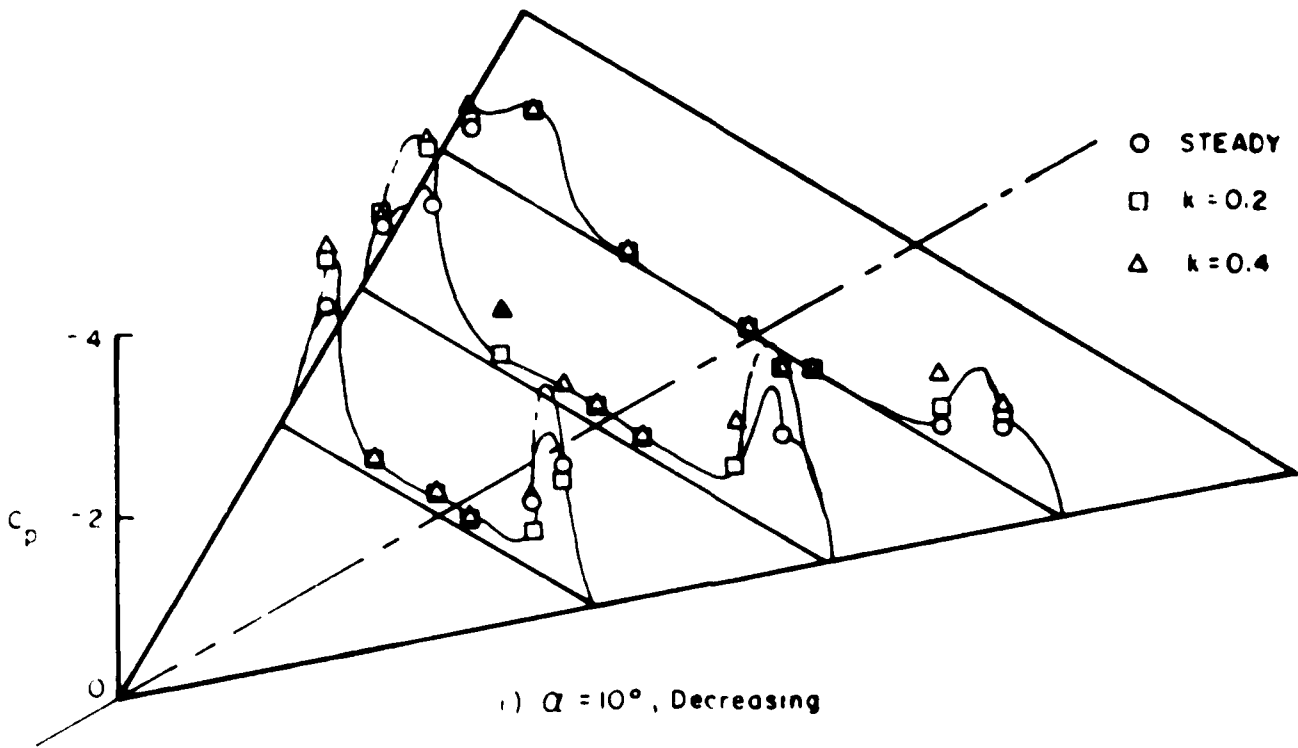
c)  $Q = 20^\circ$ , increasing



d)  $Q = 23^\circ$

Fig. 37 (continued)





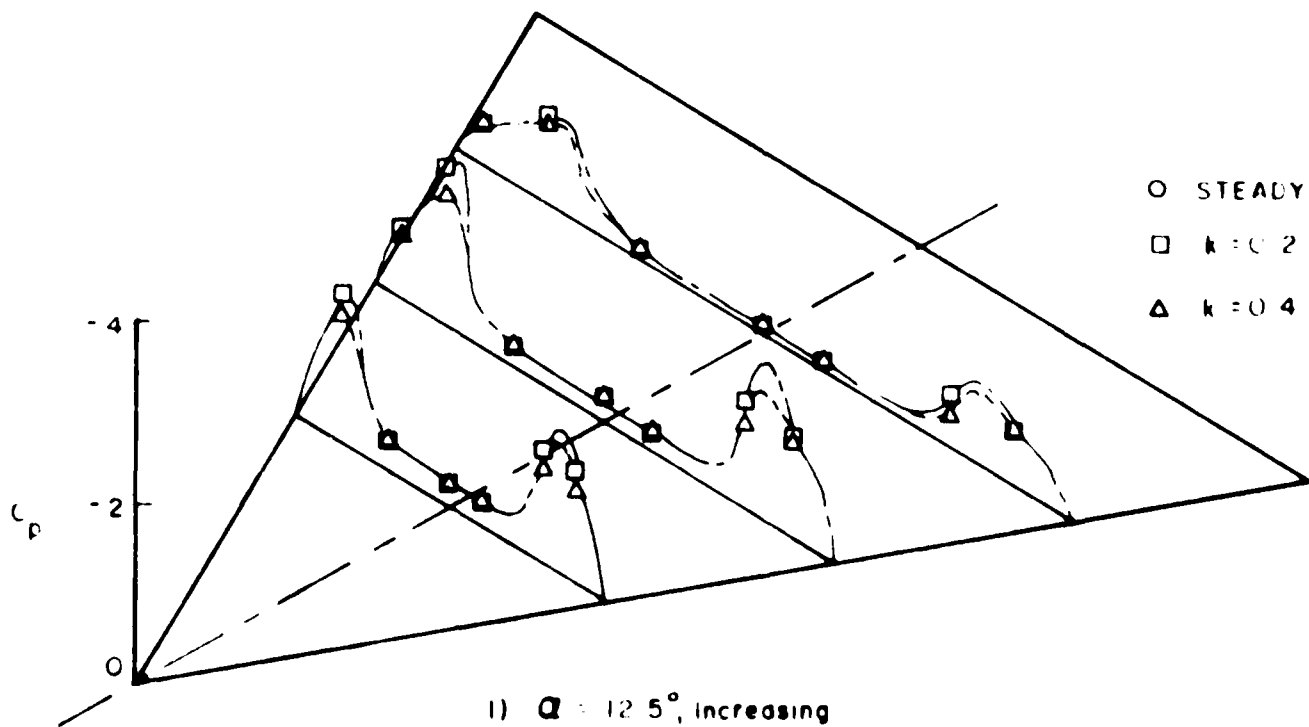
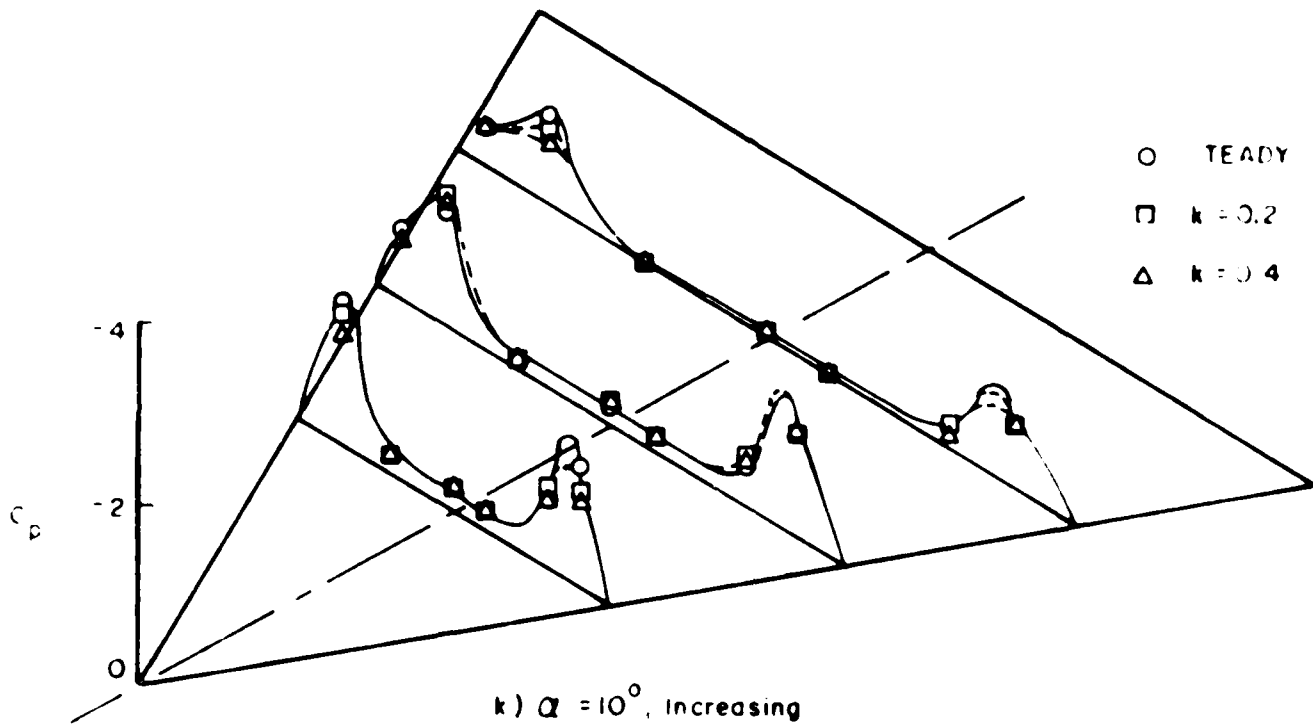


(Fig. 37 continued)

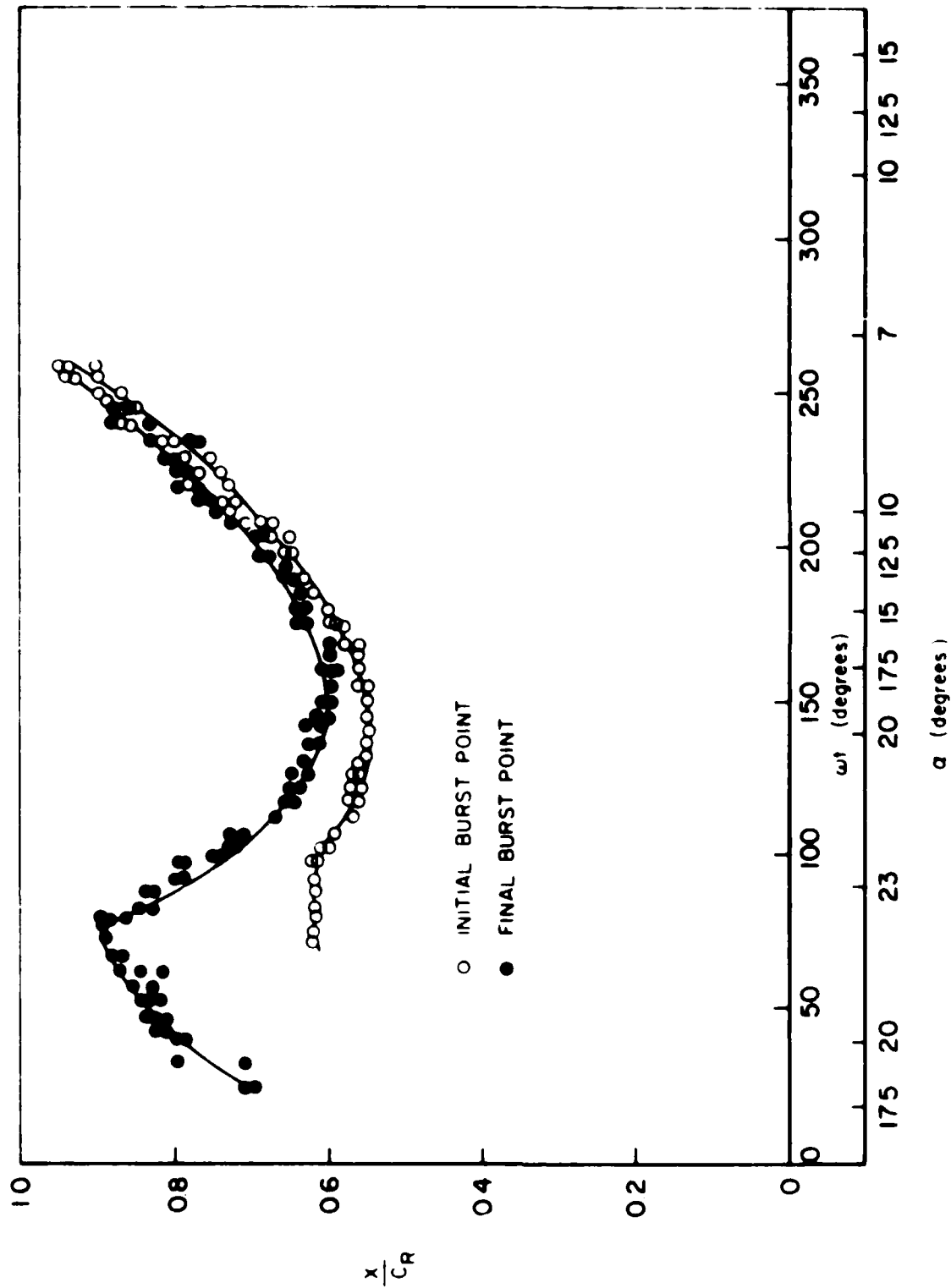
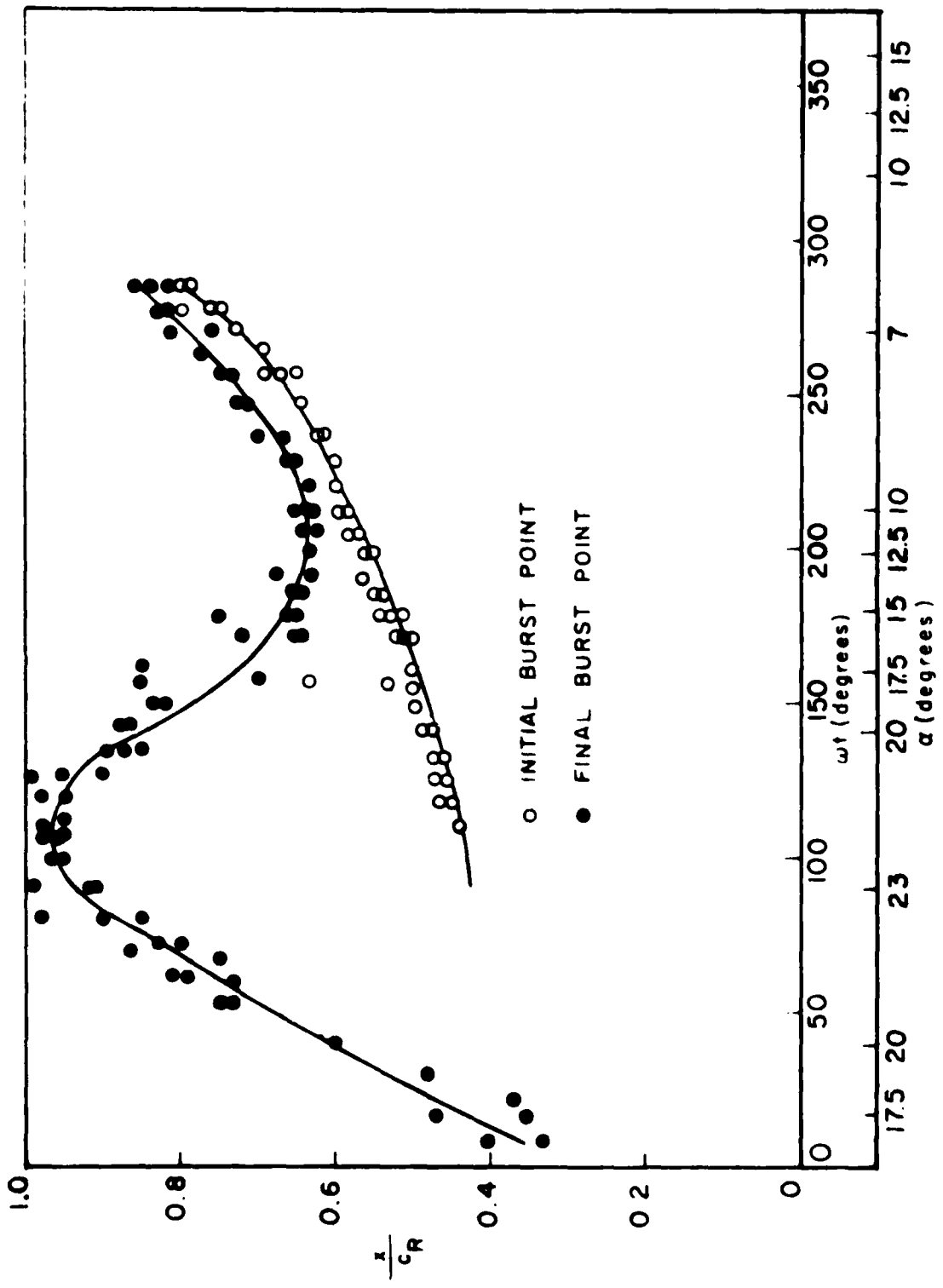


FIG. 30. INITIAL BURST POINT



RELATIONSHIP BETWEEN BURST POINT AND WEIGHT